

## Response to the Editor

We are thankful to prof. Zehe for his supervision of the review process, which have certainly improved the manuscript. The response to the individual comments is given below. The original remarks are quoted in *italics*, whereas our response is given in **bold**.

5

**(1)** *I am delighted to let you know that both reviewers are pleased with the revised version of your manuscript. Reviewer 2 recommends a few technical corrections, which I believe you are willing to implement. In line with her/him I suggest that you might consult the references listed below and optionally refer to those in case you find them or relevance.*

10 *Sasaki, Y., J. Kim, and S. Cho, 2010, Multidimensional inversion of loop-loop frequency domain EM data for resistivity and magnetic susceptibility: Geophysics, 75, 213-223.*

*Guillemoteau, J., F. X. Simon, E. Luck, and J. Tronicke, 2016, 1D sequential inversion of portable multi-configuration electromagnetic induction data: Near Surface Geophysics, 14, 411-420.*

15

*Noh, K., K. H. Lee, S. Oh, S. J. Seol, and J. Byun, 2017, Numerical evaluation of active source magnetics as a method for imaging high-resolution near-surface magnetic heterogeneity: Geophysics, 82, J27-J38.*

**As suggested, in the new version of the manuscript we included the additional references.**

20 **Moreover, in the revised manuscript, we carefully considered the recommendations provided by Reviewer #2 and provided a point-by-point reply to her/his suggestions.**

## Response to Reviewer #2

We thank Reviewer #2 for his/her valuable comments and suggestions. The response to the individual comments is given below. The original review is quoted in *italics*, whereas our response is given in **bold**.

5 **(1)** *I have few additional minor-moderate recommendations.*

*The authors added the data plots so that the readers can now properly evaluate the quality of the geophysical data and their inversion.*

*In Figures 2 and 4, I nevertheless recommend decreasing the upper limit of the color-bar to 0.05-0.06 S/m. For now, the color-scale gives the impression that the smooth solution is rather homogeneous, which, sometimes, is not true: it is just*

10 *varies within the blue color range.*

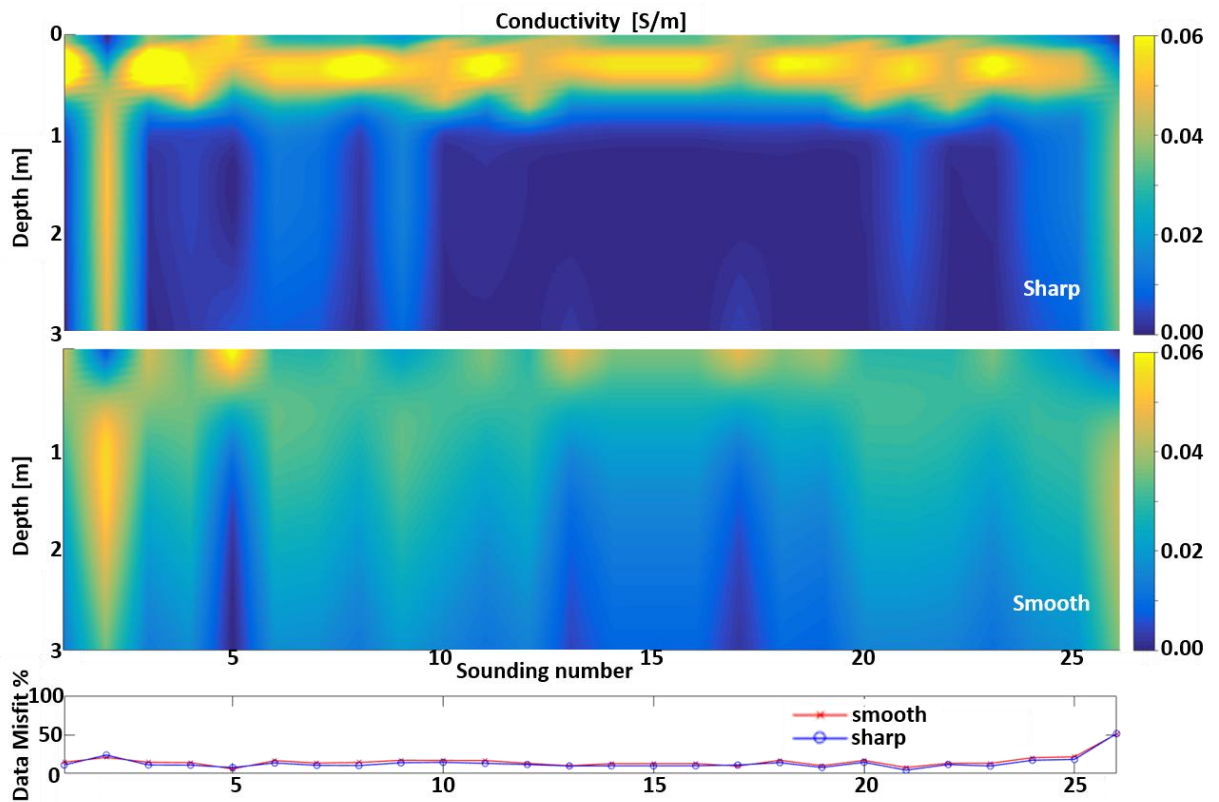


Figure R2: Examples of sharp and smooth inversions applied to the dataset 100-6dS. The results are shown together with their corresponding data misfit.

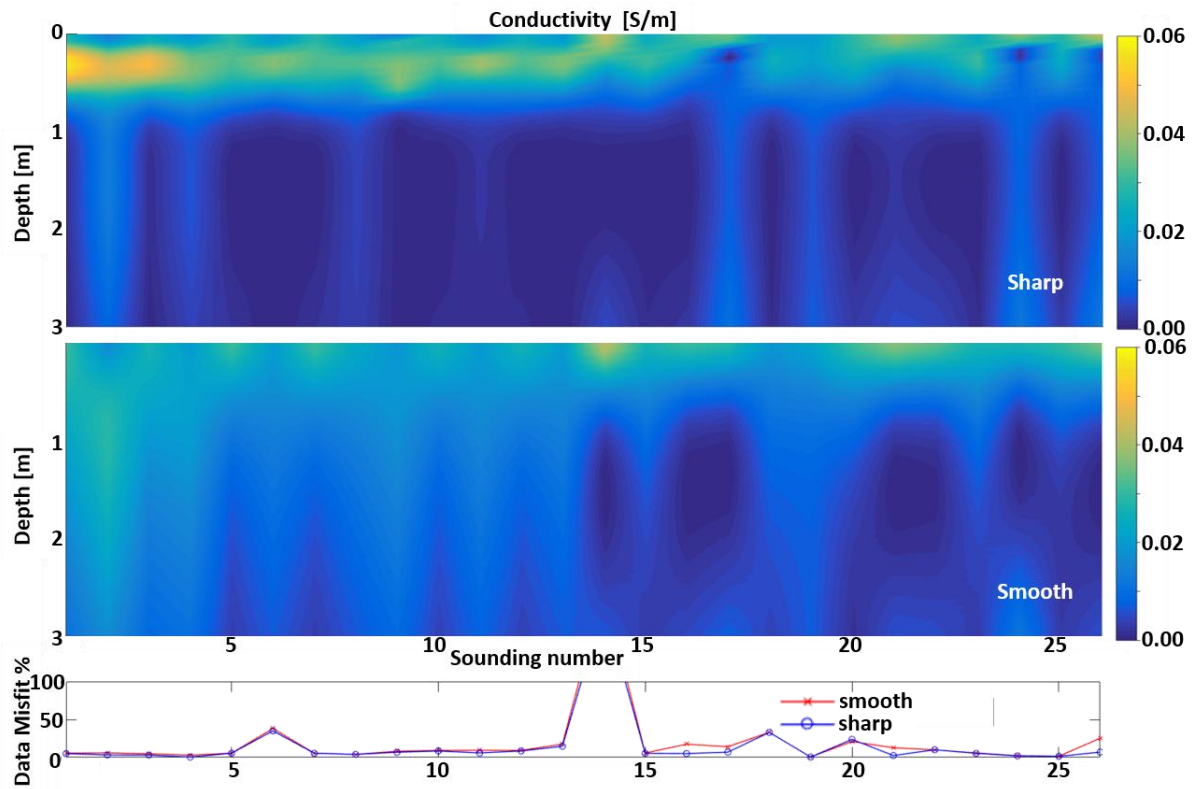


Figure R4: Examples of sharp and smooth inversions applied to the dataset 50-6dS. The results are shown together with their corresponding data misfit.

We definitely see the Reviewer's point.

However, as it can be noticed from the Fig. R2 and R4 in the present document, reducing the upper limit in the colour scale of the original Figs 2 and 4 in the manuscript will not change the impression of quite homogeneous smooth results. On the other hand, setting to 0.06 S/m the maximum value may lead to the wrong conclusion that the sharp inversion results are characterized by much higher values. Because of these reasons, we believe that it is fairer to leave the Figs 2 and 4 in the manuscript as they are now.

(2) The authors modified Figure 10, which now shows the results for different irrigation contexts. This is good. However, it would be helpful to have a discussion of the results according to what is expected from the experimental set-up. Ideally, the filtered 26 3-levels TDR soundings could be shown together with these results.

Following the Reviewer's suggestion, we added a discussion on this matter in the new version of the paper. In this respect, please, check lines 478-493 in the revised manuscript. Regarding the possibility to add a new figure, we think

that it would not be very informative as all the spatial information in the original TDR data are lost in the statistical calculation of the calibration parameters. Hence, all the relevant pieces of information are included (and plotted) in the original Figs 8 and 9 in the paper, and, actually, adding a further figure with the four filtered TDR profiles might be misleading for the reader.

5

**(3)** *On p. 13, the authors decided to discuss the analysis of the subsurface magnetic permeability. There is a recent growing interest for this topic, especially for small ground EMI devices. Hence, the recent literature should not be omitted. Before Deidda et al, (2017), please incorporate the following references from several research groups working on this topic:*

10 *Sasaki, Y., J. Kim, and S. Cho, 2010, Multidimensional inversion of loop-loop frequency domain EM data for resistivity and magnetic susceptibility: Geophysics, 75, 213-223.*

*Guillemoteau, J., F. X. Simon, E. Luck, and J. Tronicke, 2016, 1D sequential inversion of portable multi-configuration electromagnetic induction data: Near Surface Geophysics,14, 411-420.*

15

*Noh, K., K. H. Lee, S. Oh, S. J. Seol, and J. Byun, 2017, Numerical evaluation of active source magnetics as a method for imaging high-resolution near-surface magnetic heterogeneity: Geophysics, 82, J27-J38.*

**We completely agree with the Reviewer's suggestion.**

20 **Consistently, in the revised paper we added the three mentioned references.**

## Response to the Editor

We are thankful to prof. Zehe for his supervision of the review process, which have certainly improved the manuscript. The response to the individual comments is given below. The original remarks are quoted in *italics*, whereas our response is given in **bold**.

5

**(1)** *I am delighted to let you know that both reviewers are pleased with the revised version of your manuscript.*

*Reviewer 2 recommends a few technical corrections, which I believe you are willing to implement. In line with her/him I suggest that you might consult the references listed below and optionally refer to those in case you find them or relevance.*

10 *Sasaki, Y., J. Kim, and S. Cho, 2010, Multidimensional inversion of loop-loop frequency domain EM data for resistivity and magnetic susceptibility: Geophysics, 75, 213-223.*

*Guillemoteau, J., F. X. Simon, E. Luck, and J. Tronicke, 2016, 1D sequential inversion of portable multi-configuration electromagnetic induction data: Near Surface Geophysics,14, 411-420.*

15

*Noh, K., K. H. Lee, S. Oh, S. J. Seol, and J. Byun, 2017, Numerical evaluation of active source magnetics as a method for imaging high-resolution near-surface magnetic heterogeneity: Geophysics, 82, J27-J38.*

**As suggested, in the new version of the manuscript we included the additional references.**

20 **Moreover, in the revised manuscript, we carefully considered the recommendations provided by Reviewer #2 and, in a separate document, provided a point-by-point reply to her/his suggestions.**

## Response to Reviewer #2

We thank Reviewer #2 for his/her valuable comments and suggestions. The response to the individual comments is given below. The original review is quoted in *italics*, whereas our response is given in **bold**.

5 **(1)** *I have few additional minor-moderate recommendations.*

*The authors added the data plots so that the readers can now properly evaluate the quality of the geophysical data and their inversion.*

*In Figures 2 and 4, I nevertheless recommend decreasing the upper limit of the color-bar to 0.05-0.06 S/m. For now, the color-scale gives the impression that the smooth solution is rather homogeneous, which, sometimes, is not true: it is just*

10 *varies within the blue color range.*

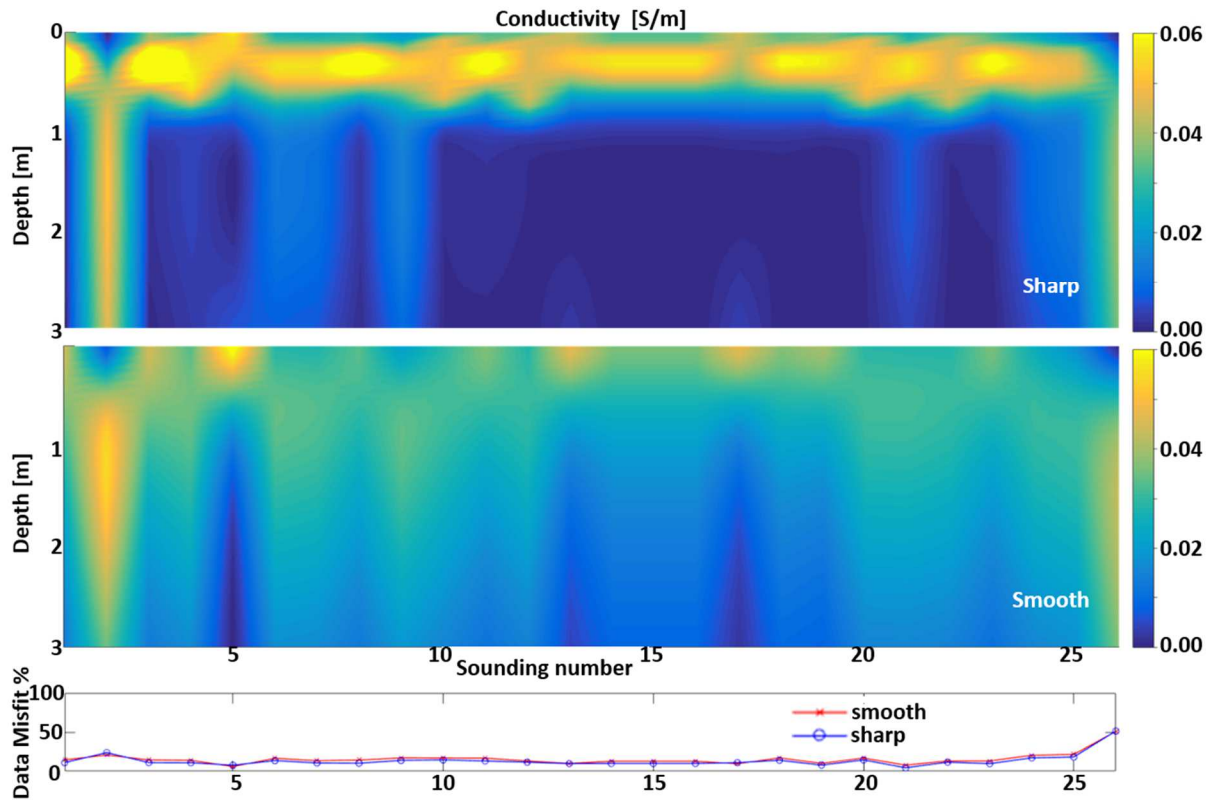


Figure R2: Examples of sharp and smooth inversions applied to the dataset 100-6dS. The results are shown together with their corresponding data misfit.

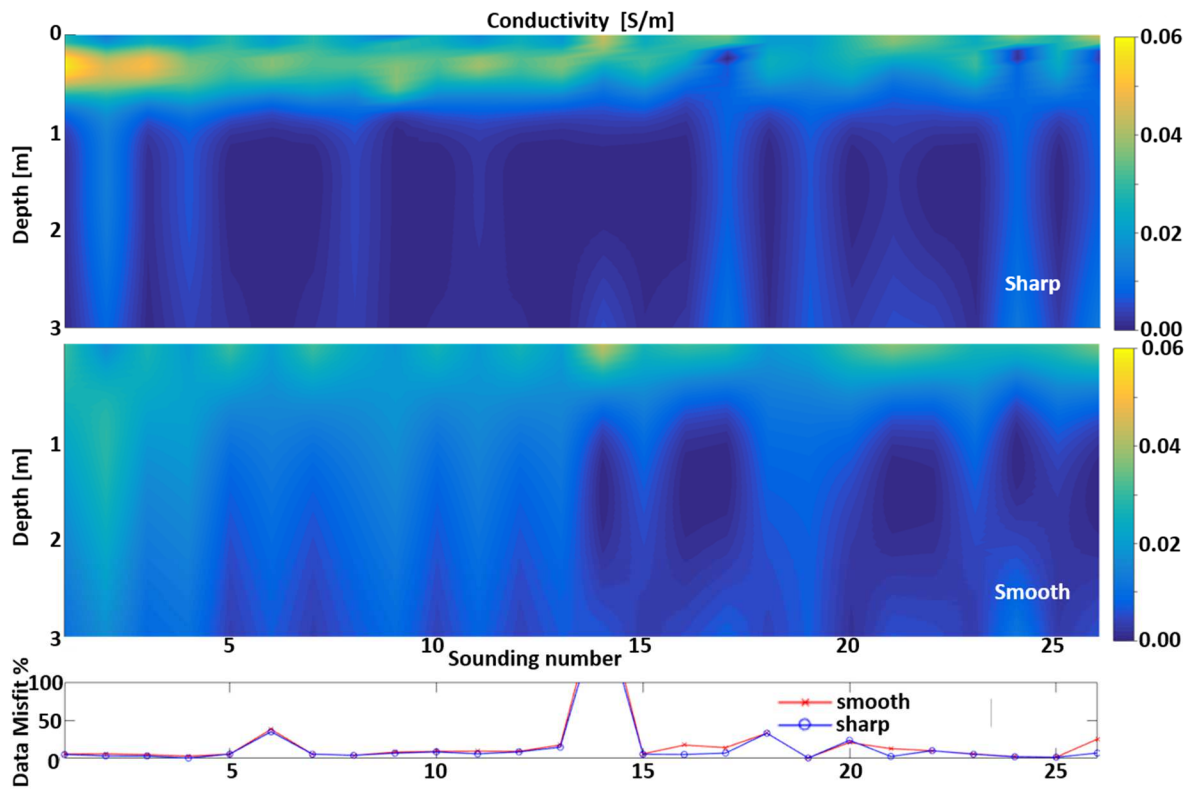


Figure R4: Examples of sharp and smooth inversions applied to the dataset 50-6dS. The results are shown together with their corresponding data misfit.

We definitely see the Reviewer's point.

However, as it can be noticed from the Fig. R2 and R4 in the present document, reducing the upper limit in the colour scale of the original Figs 2 and 4 in the manuscript will not change the impression of quite homogeneous smooth results. On the other hand, setting to 0.06 S/m the maximum value may lead to the wrong conclusion that the sharp inversion results are characterized by much higher values. Because of these reasons, we believe that it is fairer to leave the Figs 2 and 4 in the manuscript as they are now.

(2) The authors modified Figure 10, which now shows the results for different irrigation contexts. This is good. However, it would be helpful to have a discussion of the results according to what is expected from the experimental set-up. Ideally, the filtered 26 3-levels TDR soundings could be shown together with these results.

Following the Reviewer's suggestion, we added a discussion on this matter in the new version of the paper. In this respect, please, check lines 478-493 in the revised manuscript. Regarding the possibility to add a new figure, we think

that it would not be very informative as all the spatial information in the original TDR data are lost in the statistical calculation of the calibration parameters. Hence, all the relevant pieces of information are included (and plotted) in the original Figs 8 and 9 in the paper, and, actually, adding a further figure with the four filtered TDR profiles might be misleading for the reader.

5

**(3)** *On p. 13, the authors decided to discuss the analysis of the subsurface magnetic permeability. There is a recent growing interest for this topic, especially for small ground EMI devices. Hence, the recent literature should not be omitted. Before Deidda et al, (2017), please incorporate the following references from several research groups working on this topic:*

10 *Sasaki, Y., J. Kim, and S. Cho, 2010, Multidimensional inversion of loop-loop frequency domain EM data for resistivity and magnetic susceptibility: Geophysics, 75, 213-223.*

*Guillemoteau, J., F. X. Simon, E. Luck, and J. Tronicke, 2016, 1D sequential inversion of portable multi-configuration electromagnetic induction data: Near Surface Geophysics,14, 411-420.*

15

*Noh, K., K. H. Lee, S. Oh, S. J. Seol, and J. Byun, 2017, Numerical evaluation of active source magnetics as a method for imaging high-resolution near-surface magnetic heterogeneity: Geophysics, 82, J27-J38.*

**We completely agree with the Reviewer's suggestion.**

20 **Consistently, in the revised paper we added the three mentioned references.**

1 **CALIBRATING ELECTROMAGNETIC INDUCTION CONDUCTIVITIES WITH TIME-DOMAIN**

2 **REFLECTOMETRY MEASUREMENTS**

3 Dragonetti<sup>1</sup> Giovanna, Alessandro Comegna<sup>2</sup>, Ali Ajeel<sup>2</sup>, Gian Piero Deidda<sup>3</sup>, Nicola  
4 Lamaddalena<sup>1</sup>, Giuseppe Rodriguez<sup>4</sup>, Giulio Vignoli<sup>3,5</sup>, Antonio Coppola<sup>2\*</sup>

5

6 (1) Mediterranean Agronomic Institute (MAIB) - Land & Water Department, Valenzano (Bari),  
7 Italy

8 (2) University of Basilicata, School of Agricultural, Forestry and Environmental Sciences -  
9 Hydraulics and Hydrology Division, Potenza, Italy. e-mail: antonio.coppola@unibas.it

10 (3) Dipartimento di Ingegneria Civile, Ambientale e Architettura, Università di Cagliari, Cagliari,  
11 Italy

12 (4) Dipartimento di Matematica e Informatica, Università di Cagliari, Cagliari, Italy

13 (5) Groundwater and Quaternary Geology Mapping Department, Geological Survey of Denmark  
14 and Greenland, Aarhus, Denmark

15

16 **Abstract**

17 This paper deals with the issue of monitoring the spatial distribution of bulk electrical  
18 conductivity  $\sigma_b$ , in the soil root zone by using Electromagnetic Induction (EMI) sensors under  
19 different water and salinity conditions. To deduce the actual distribution of depth-specific  $\sigma_b$   
20 from EMI apparent electrical conductivity ( $EC_a$ ) measurements, we inverted the data by using a  
21 regularized 1D inversion procedure designed to manage nonlinear multiple EMI-depth  
22 responses. The inversion technique is based on the coupling of the damped Gauss-Newton  
23 method with truncated generalized singular value decomposition (TGSVD). The ill-posedness of  
24 the EMI data inversion is addressed by using a sharp stabilizer term in the objective function.

25 This specific stabilizer promotes the reconstruction of blocky targets, thereby contributing to  
26 enhance the spatial resolution of the EMI results in presence of sharp boundaries (otherwise  
27 smeared out after the application of more standard, Occam-like regularization strategies  
28 searching for smooth solutions). Time-Domain Reflectometry (TDR) data are used as ground-  
29 truth data for calibration of the inversion results. An experimental field was divided into four  
30 transects 30 m long and 2.8 m wide, cultivated with green bean and irrigated with water at two  
31 different salinity levels and using two different irrigation volumes. Clearly, this induced  
32 different salinity and water contents within the soil profiles. For each transect, 26 regularly  
33 spaced monitoring soundings (1 m apart) were selected for the collection of, respectively: (i)  
34 Geonics EM-38 and (ii) Tektronix Reflectometer data. Despite the original discrepancies in the  
35 EMI and TDR data, we found a significant correlation of the means and standard deviations of  
36 the two data series, in particular, after a low-pass spatial filtering of the TDR data. Based on  
37 these findings, the paper introduces a novel methodology to calibrate EMI-based electrical  
38 conductivities via TDR direct measurements. This calibration strategy consists in a linear  
39 mapping of the original inversion results into a new conductivity spatial distribution with the  
40 coefficients of the transformation uniquely based on the statistics of the two original  
41 measurement datasets (EMI and TDR conductivities).

42

### 43 **Introduction**

44 Soil water content and salinity vary in space both vertically and horizontally. Their distribution  
45 depends on management practices and on the complex nonlinear processes of soil water flow  
46 and solute transport, resulting in variable storages of solutes and water (Coppola et al. 2015).  
47 Monitoring the actual distribution of water and salts in the soil profile explored by roots is  
48 crucial for managing irrigation with saline water, while still maintaining an acceptable crop

49 yield. For water and salts monitoring over large areas, there are now non-invasive techniques  
50 based on electromagnetic sensors which allow the bulk electrical conductivity of soils  $\sigma_b$  to be  
51 determined (Sheets and Hendrickx 1995, Corwin and Lesch 2005, Robinson et al. 2012,  
52 Doolittle and Brevik 2014, Von Hebel et al. 2014, among many others).

53  $\sigma_b$  depends on: (i) soil water content  $\theta$ ; (ii) electrical conductivity of the soil solution (salinity)  
54  $\sigma_w$ ; (iii) tortuosity of the soil-pore system  $\tau$ ; and (iv) other factors related to the solid phase such  
55 as bulk density, clay content and mineralogy.

56 Electromagnetic induction (EMI) sensors provide measurements of the depth-weighted  
57 apparent electrical conductivity  $EC_a$  accordingly to the specific distribution of the bulk electrical  
58 conductivity  $\sigma_b$  as well as the depth response function of the sensor used (McNeill 1980). Thus,  
59 the dependence on  $\sigma_b$  makes  $EC_a$  sensitive to soil salinity and water distributions. In principle,  
60 specific procedures for estimating salinity and water content may be developed through  
61 controlled laboratory experiments where  $\sigma_b$ ,  $\sigma_w$  and  $\theta$  are measured simultaneously (Rhoades  
62 and Corwin 1981). That said, to monitor salinity and water content, it is crucial to correctly infer  
63 the depth-distribution of  $\sigma_b$  from profile-integrated  $EC_a$  readings. To date, this issue has been  
64 tackled by applying two different strategies: The first is to use empirical calibration relations  
65 relating the depth-integrated  $EC_a$  readings to the  $\sigma_b$  values measured by alternative methods -  
66 like Time-Domain Reflectometry (TDR) - within discrete depth intervals (Rhoades and Corwin,  
67 1981; Lesch et al., 1992; Triantafyllis et al., Laslett, and McBratney 2000; Amezketa, 2006;  
68 Yao and Yang, 2010; Coppola et al. 2016); The second consists in the 1D inversion of the  
69 observations from the EMI sensor to reconstruct the vertical conductivity profile (Borchers,  
70 Uram, and Hendrickx et al., 1997; Hendrickx et al., 2002; Santos et al., 2010; Lavoué et al.,  
71 2010; Mester et al., 2011; Minsley et al., 2012; Deidda, Fenu, and Rodriguez et al., 2014;  
72 Von Hebel et al., 2014).

73 With regard to  $EC_a$  inversion, a forward model still commonly used is the cumulative response  
74 model or local-sensitivity model (LSM) (McNeill, 1980). McNeill's linear approach is well suited  
75 to the cases characterized by an induction number  $B$  (defined as the ratio between the coil  
76 distance and the skin depth) much smaller than 1. However, because of the increasing  
77 computing power, improved forward modeling algorithms based on more accurate nonlinear  
78 approaches are becoming increasingly common (Hendrickx et al., 2002; Deidda, Fenu, and  
79 Rodriguez et al., 2014; Deidda, Bonomi, and Manzi et al., 2003; Lavoué et al., 2010; Santos et  
80 al., 2010). For example, these more sophisticated forward modeling codes can cope with a  
81 wider range of conductivities for which the assumption  $B \ll 1$  is not necessarily met.

82 To obtain reliable vertical distributions of electrical conductivity, the  $EC_a$  data used for the  
83 inversion should consist of multi-configuration data. Hence, data collection should be  
84 performed either with the simultaneous use of different sensors or with different acquisition  
85 configurations with only one sensor (different configurations may consist, e.g., in different coil  
86 orientations, varying intercoil separations and/or frequencies – see, for example Díaz de Alba  
87 and Rodriguez, 2016). Multi-configuration data can be effectively used to invert for vertical  
88 electrical conductivity profiling since the  $EC_a$  measures actually investigate different,  
89 overlapping soil volumes. Devices specifically designed for the simultaneous acquisition of  
90 multi-configuration data are currently available. Some of them consist of one transmitter and  
91 several receivers with different coil separations and orientations (Santos et al., 2010). If,  
92 instead, a sensor with single intercoil distance and frequency is available, a possible alternative  
93 to having multi-configuration measurements could be to record the data at different heights  
94 above the ground.

95 Unfortunately, like every other physical measurement, frequency-domain electromagnetic  
96 measurements are sensitive to noise that is very hard to model effectively. Moreover as

97 discussed, for example, in Lavoué et al. (2010), Mester et al. (2011), and Von Hebel et al.  
98 (2014), an instrumental shift in conductivity values could be observed due to system  
99 miscalibration and the influence of surrounding conditions such as temperature, solar  
100 radiation, power supply conditions, the presence of the operator, zero-leveling procedures,  
101 cables close to the system and/or the field setup (see, amongst others, Sudduth, ~~Drummond,~~  
102 ~~and Kitchen et al.,~~ 2001; Robinson et al., 2004; Abdu, ~~Robinson, and Jones et al.,~~ 2007; Gebbers  
103 et al., 2009; Nüsch et al., 2010). Hence, the EC<sub>a</sub> data from EMI measurements would generally  
104 require a proper calibration. One option could be to use soil cores as ground-truth data. In this  
105 case, EC<sub>a</sub> measurements at the sampling locations can be compared against EC<sub>a</sub> data predicted  
106 by the theoretical forward response applied to the true electrical conductivity distribution  
107 measured directly on the soil cores (Triantafyllis ~~et al., Laslett, and McBratney~~ 2000, ~~;~~  
108 Moghadas et al., 2012). Clearly, this strategy is extremely time- (and resource-) consuming. To  
109 avoid drilling, Lavoué et al. (2010) introduced a calibration method, later also adopted by  
110 Mester et al. (2011) and Von Hebel et al. (2014), using the electrical conductivity distribution  
111 obtained from Electrical Resistivity Tomography (ERT) data as input for electromagnetic  
112 forward modeling. The EC<sub>a</sub> values predicted on the basis of ERT data were used to remove the  
113 observed instrumental shift and correct the measured conductivity values by linear regression.  
114 However, in general, a prerequisite for such an approach concerns the reliability of the  
115 inversion of the ERT result. This is not only due to the quality of the original data, but also the  
116 adopted inversion procedure. Indeed, ERT inversion is an ill-posed problem: its solutions are  
117 characterized by non-uniqueness and instability with respect to the input data (Yu and  
118 Dougherty 2000; Zhdanov 2002; Günther 2011). In the Tikhonov regularization framework, ill-  
119 posedness is addressed by including the available prior information. Such information can be  
120 very general. For example, it can be geometrical (i.e., associated to the presence of smooth or

121 sharp boundaries between different lithologies). Obviously, the final result largely reflects the  
122 initial guess formalized via the chosen regularization term (Pagliara and Vignoli 2006; Günther  
123 2011; Vignoli, Deiana, and Cassiani 2012; Fiandaca et al. 2015).

124 When relatively shallow depths have to be explored (1-2m), direct soil sampling and ERT can be  
125 effectively replaced by TDR observations. TDR devices are designed to measure the dielectric  
126 properties of soils. More precisely, they measure the apparent electrical permittivity, from  
127 which, not only the dielectric constant, but also the effective electrical conductivity can be  
128 deduced (e.g., Dalton et al., 1984; Topp et al., 1988; Weerts et al., 2001; Noborio, 2001; Jones  
129 et al., 2002; Robinson et al., 2003; Lin et al., 2007; Thomsen et al., 2007; Huisman et al., 2008;  
130 Lin et al., 2008; Koestel et al., 2008; Bechtold et al., 2010). In general, TDR measurements might  
131 be difficult to be used to recover the electrical conductivity with the desired accuracy.  
132 However, in the literature, many examples are reported in which, within the range 0.002 – 0.2  
133 S/m (compatible with the examples investigated in the present research), and by properly using  
134 the TDR device (e.g., by paying attention ~~to minimize to~~ to minimize the effects of nonparallel  
135 device rods inserted into the ground), the TDR conductivity can be measured with an  
136 uncertainty level lower than 5% (e.g.: Huisman et al., 2008; Bechtold et al., 2010). Besides,  
137 since the TDR measurements are commonly calibrated in saline solutions just before the field  
138 data acquisitions, they could potentially provide a reliable, absolute estimation of the actual  
139 ground conductivity (Ferré et al., 1998a). For this reason, in some cases, TDR observations have  
140 been proposed as a valid tool for ground ~~truthing~~ truthing the ERT and, possibly, as  
141 ancillary information source to constraint for the ERT inversions (Koestel et al., 2008). For  
142 additional studies dealing with the use of ERT data for the validation of the EMI and TDR  
143 measurements for soil characterization we refer the reader to, for ~~example, Cassiani~~ example,  
144 Cassiani et al. (2012), and Ursino et al. (2014).

145 In the present research, we focus on the use of TDR data to absolute calibrate the  
146 conductivities obtained by inverting the EMI measurements. To do this, a dataset collected  
147 during an experiment carried out along four transects under different salinity and water  
148 content conditions (and monitored with both EMI and TDR sensors) is utilized. We first tackle  
149 the problem of inferring the soil electrical conductivity distribution from multi-height  $EC_a$   
150 readings via the proper inversion strategy. Then we assess the quality of these reconstructions  
151 by using TDR data as ground-truth. In this respect, in the following, we discuss how to  
152 effectively compare the  $\sigma_b$  values generated by the EMI inversion with the associated TDR  
153 values. In fact, as discussed by Coppola et al. (2016), because of their relatively smaller  
154 observation volume, TDR data provide quasi-pointlike measurements and do not integrate the  
155 small-scale variability (of soil water content, solute concentrations, etc.) induced by natural soil  
156 heterogeneity. By contrast, EMI data necessarily overrule the small-scale heterogeneities seen  
157 by TDR probes as they investigate a much larger volume. Accordingly, the paper provides a  
158 methodology to calibrate EMI results by TDR readings. This procedure lies in conditioning the  
159 original TDR data and in the statistical characteristics of the two EMI and TDR data series. On  
160 the basis of the proposed analysis, we discuss the physical reasons for the differences between  
161 EMI and TDR-based bulk electrical conductivity and identify a method to effectively migrate the  
162 reliable TDR information across the larger volume investigated by EMI.

163

## 164 **Materials and Methods**

165 The experiment was carried out at the Mediterranean Agronomic Institute of Bari (MAIB) in  
166 south-eastern Italy. The soil was pedologically classified as Colluvic Regosol, consisting of a  
167 silty-loam layer of an average depth of 0.6 m on fractured calcarenite bedrock. The  
168 experimental set-up (Fig. 1) consisted of four transects of 30 m length and 2.8 m width,

169 equipped with a drip irrigation system with five dripper lines placed 0.35 m apart and  
170 characterized by an inter-dripper distance of 0.2 m. The dripper discharge was 2 l/h. Green  
171 beans were grown in each transect. The irrigation volumes were calculated according to the  
172 time-dynamics of water content in the first 0.25 m measured by a TDR probe inserted vertically  
173 at the soil surface. TDR readings were taken: (i) just before and (ii) two hours after every  
174 irrigation. Based on the difference between the water content at field capacity and that  
175 measured just before irrigation, it was easy to assess the volumes needed to bring the soil  
176 water content back to the field capacity.

177 The four transects were irrigated with water at two different salinity levels and with two  
178 different water volumes. Transect 1: 100% of the irrigation water at 1 dSm<sup>-1</sup> (hereafter 100-  
179 1dS); Transect 2: 50% of irrigation water at 1 dSm<sup>-1</sup> (50-1dS); Transect 3: 100% of the irrigation  
180 water at 6 dSm<sup>-1</sup> (100-6dS); Transect 4: 50% of irrigation water at 6 dSm<sup>-1</sup> (50-6dS). Water  
181 salinity was induced by adding calcium chloride (CaCl<sub>2</sub>) to tap water. Irrigation volumes were  
182 applied every two days.

183 EMI readings - in vertical magnetic dipoles configurations - were collected by using a Geonics  
184 EM38 device (Geonics Limited, Ontario, Canada). The EM38 operates at a frequency of 14.6 kHz  
185 with a coil spacing of 1 m, and with a nominal measurement depth of ~1.5 m (McNeill, 1980).  
186 The lateral footprint of the EM38 measurement can be considered approximately equal to the  
187 vertical one. Thus, the  $\sigma_b$  seen by the EMI, in a given depth-layer, necessarily differs from that  
188 seen by a TDR probe at the same depth-layer, due to the very different spatial resolutions.

189 At the beginning of the measurement campaign, the EMI sensor was “nulled” according to the  
190 manufacturer’s manual. Readings were taken just after each irrigation application at 1 m step,  
191 along the central line of each transect, for an overall total of 26 soundings per transect. Multi-  
192 height EM38 readings were acquired at heights of 0.0, 0.2, 0.4 and 0.6 m from the ground.

193 Taking measurements just after irrigation allowed relatively time-stable water contents to be  
194 assumed at each site throughout the monitoring phases.

195 Just after the EM38 measurements, a TDR probe was inserted vertically at the soil ~~surface~~  
196 ~~insurface in~~ 26 locations, each corresponding to the central point of an EM38 reading. A  
197 Tektronix 1502C cable tester (Tektronix Inc., Baverton, OR) was used in this study. It enables  
198 simultaneous measurement of water content  $\theta$  and bulk electrical conductivity  $\sigma_b$  of the soil  
199 volume explored by the probe (Heimovaara et al., 1995; Robinson and Friedman, 2003;  
200 Coppola et al., 2011; Coppola et al., 2015). The TDR transmission line consisted of an antenna  
201 cable (RG58, 50  $\Omega$  characteristic impedance, 2 m long and with 0.2  $\Omega$  connector impedance)  
202 and three-wire probes, 0.25 m long, 0.07 m internal distance, and 0.005 m in diameter. The  
203 TDR probe was not embedded permanently at fixed depths along the soil profile to avoid any  
204 potential disturbance to the EMI acquisitions. The TDR readings were taken at three different  
205 depth intervals (0.0-0.2, 0.2-0.4, 0.4-0.6 m). After the measurements at the surface (0.0-0.2 m),  
206 a trench was dug up to 0.2 m depth. TDR probes were then inserted vertically for the additional  
207 collection of the data in the interval 0.2-0.4 m, after which the trench was deepened up to 0.4  
208 m and readings were taken at 0.4-0.6 m. The  $\sigma_{b,TDR}$  readings were used for the calibration of the  
209 EM38 inversion results.

210

211 Data Handling

212 *Multi-height EMI readings inversion*

213 Nonlinear 1D forward modeling, which predicts multi-height EMI readings from a loop-loop  
214 device, can be obtained by suitable simplification of Maxwell's equations that takes the  
215 symmetry of the problem into account. This approach is described in detail in (Hendrickx et al.  
216 2002), and is based on a classical approach extensively described in the literature (Wait 1982;

217 Ward and Hohmann 1988). The predicted data are functions of the electrical conductivity and  
218 the magnetic permeability in a horizontally layered medium.

219 When the coils of the recording device are vertically oriented with respect to the ground  
220 surface, the reading at height  $h$  can be expressed by using the integral:

$$-\rho^3 \int_0^{\infty} \lambda^2 e^{-2h\lambda} R_0(\lambda) J_0(\rho\lambda) d\lambda, \quad (1)$$

221 where  $\rho$  denotes the distance between the coils,  $J_0(\lambda)$  is the Bessel function of the first kind  
222 of order 0, and  $R_0(\lambda)$  is a complex valued function which depends upon the electromagnetic  
223 properties of the ground layers. A similar expression is valid also when the coils are horizontally  
224 aligned. Hence the dependence of the measured data on the electrical conductivity  $\sigma_k$ , of the  
225 (homogeneous)  $j$ -th layer is incorporated into the function  $R_0(\lambda)$ . We discretize the problem

226 with  $n$  layers whose characteristic parameters  $\sigma_j$  (with  $j = 1, \dots, n$ ) are the unknowns we  
227 invert for. In the present research, we neglect any dependence of the electromagnetic  
228 response on magnetic permeability as we assume it is fixed and equal to the permeability of  
229 empty space. In principle, it is possible to consider two measurements for each location: one  
230 for the horizontal and one for the vertical configuration of the transmitting and receiving loops.

231 In this case, the data used as inputs for the inversion are  $2 \cdot m$ , where-with  $m$  is-representing  
232 the number of heights  $h_1, h_2, \dots, h_m$  where the measurements are performed.

233 A least squares data fitting approach leads to the minimization of the function:

$$f(\sigma) = \frac{1}{2} \sum_{i=1}^{2m} r_i^2(\sigma), \quad (2)$$

234 where  $\sigma = (\sigma_1, \dots, \sigma_n)^T$ , and  $r_i^2(\sigma)$  is the misfit between the  $i$ -th measurement and the  
235 corresponding forward modeling prediction based on Eq. 1.

236 We solve the nonlinear minimization problem by the inversion procedure described in Deidda,  
237 ~~Fenu, and Rodriguez et al.~~ (2014). The algorithm is based on a damped regularized Gauss-  
238 Newton method. The problem is linearized at each iteration by means of a first order Taylor  
239 expansion. The use of the exact Jacobian (~~whose expression is detailed in Deidda, Fenu, and~~  
240 ~~Rodriguez, et al.,~~ 2014) makes the computation faster and more accurate than using a finite  
241 difference approximation. The damping parameter is determined in order to ensure both the  
242 convergence of the method and the positivity of the solution. The regularized solution to each  
243 linear subproblem is computed by the truncated generalized singular value decomposition  
244 (TGSVD - Díaz de Alba and Rodriguez, 2016) employing different regularization operators.  
245 Besides the classical regularization matrices based on the discretization of the first and second  
246 derivatives, to further improve the spatial resolution of EMI inversion results in all the cases  
247 characterized by sharp interfaces, we tested a nonlinear regularization stabilizer promoting the  
248 reconstruction of blocky features (Zhdanov, Vignoli, and Ueda 2006; Ley-Cooper et al. 2015;  
249 Vignoli et al. 2015; Vignoli et al. 2017). The advantage of this relatively new regularization is  
250 that, when appropriate prior knowledge about the medium to reconstruct is available, it can  
251 mitigate the smearing and over-smoothing effects of the more standard inversion strategies.  
252 This, in turn, can make the calibration of the EMI data against the TDR data more effective. For  
253 this reason, in the following, the EMI results used for our assessments are those inferred by  
254 means of this sharp inversion. The differences between the “standard” smooth (based on the  
255 first derivative) reconstruction and the sharp one are clearly shown in Fig.s 2 and 4. In all cases,  
256 the inversions are performed with a 100-layer homogeneous discretization, down to 8 m, with  
257 fix interfaces. We opted for such a parameterization to be able to: (i) control the inversion  
258 results by acting merely on the regularization parameters, and (ii) remove the regularization  
259 effects possibly originated by the discretization choice (e.g., the number of layers, interfaces

260 locations). In this way, it was possible to use an automatic strategy for the selection of the  
261 regularization parameters. In Fig.s 2 and 4, the sharp results (upper panels) associated with the  
262 cases 100-6dS and 50-6dS are compared against the corresponding smooth inversions (middle  
263 panels). Even if the data misfit levels largely match (lower panels in Fig.s 2 and 4, but also Fig.s  
264 3 and 5), the two inversion strategies produce reconstructions that differ significantly. This is  
265 due to the inherent ill-posedness of the EMI inversion. By considering solely the geophysical  
266 observations, it is impossible to decide which model is the best. In this research, based on the  
267 fact that, just after the irrigation, the effect of the water is supposed to remain localized in the  
268 shallowest portion of the soil section, the sharp inversion was found to provide more reliable  
269 results. Moreover, to some extent, the general better agreement of the data calculated from  
270 the sharp model supports the idea that the electrical properties distributions are better  
271 inferred via the sharp regularization. In any case, since in this research we calibrate the EMI-  
272 derived models (and not the data), the final calibrated result will reflect the assumptions made  
273 in the first place, when the EMI data are inverted (specifically, the regularization assumptions).  
274 A possible alternative way to still effectively use the TDR data to calibrate the EMI  
275 measurements (and not the associated conductivity model) could consist in performing the  
276 calibration in the data-space (and not in the model-space). In ~~this~~ the data-space  
277 calibration, the measured TDR conductivity could be used as input model to calculate the  
278 EC<sub>a</sub> response of the EMI device actually used. In turn, this calculated EC<sub>a</sub> response can be  
279 compared against the measured EMI data and used for their calibration. However, eventually,  
280 also this latter data-space calibration will have to deal with the inversion issues once the  
281 calibrated EMI data need to be converted into conductivities  $\sigma_b$ . In this paper, we chose the  
282 model-space calibration strategy as, in general, in the available EMI inversion codes, it is not  
283 always easy to decouple the forward modelling routines from the overall inversion algorithm.

284 Hence, the discussed approach could be more directly applicable and beneficial for  
285 practitioners. On the other hand, it is true that the data-space calibration naturally takes into  
286 account the scale-mismatch between the TDR and the EMI measurements with no need for any  
287 statistical calculation.

288 It is worth noting that the constant magnetic permeability assumption is not always valid.  
289 Inverting for the magnetic permeability is sometimes not only necessary, but it can also provide  
290 an additional tool for soil characterization (e.g., Beard and Nyquist, 1998; Farquharson,  
291 ~~Oldenburg, and Routh et al., 2003; Sasaki et al., 2010; Guillemoteau et al. 2016; Noh et al.~~  
292 ~~2017; Deidda, Diaz De Alba, and Rodriguez et al., 2017).~~

293 For the sake of clarity, hereafter, the  $\sigma_b$  values generated from the EMI data inversion will be  
294 identified explicitly as  $\sigma_{b,EMI}$ .

295

### 296 *TDR-based water content and bulk electrical conductivity*

297 The Tektronix 1502C can measure the total resistance  $R_t$  of the transmission line by:

$$R_t = Z_c \frac{(1 + \rho_\infty)}{(1 - \rho_\infty)} = R_s + R_c \quad (3)$$

298 where:  $R_s$  is the soil's contribution to total resistance and  $R_c$  accounts for the contribution of  
299 the series resistance from the cable; the connector  $Z_c$  is the characteristic impedance of the  
300 transmission line; and  $\rho$  is a reflection coefficient at a very long time, when the waveform has  
301 stabilized.

302 The  $\sigma_b$  value at 25°C can be calculated as (Rhoades and van Schilfgaarde 1976; Wraith et al.  
303 1993):

$$\sigma_{b, 25^\circ\text{C}} = \frac{K_c}{Z_c} f_T \quad (4)$$

304 where  $K_c$  is the geometric constant of the TDR probe and  $f_T$  is a temperature correction factor  
 305 to be used for values recorded at temperatures other than 25°C. Both  $Z_c$  and  $K_c$  can be  
 306 determined by measuring  $R_t$  with the TDR probe immersed in a solution with known  
 307 conductivity  $\sigma_b$ . Hereafter, these  $\sigma_b$  measurements will be identified as  $\sigma_{b,TDR}$ .

308

309 *Evaluation of Concordance between  $\sigma_{b,TDR}$  measurements and  $\sigma_{b,EMI}$  estimates*

310 The agreement between  $\sigma_{b,TDR}$  measurements and  $\sigma_{b,EMI}$  estimations in the 0.0-0.6 m range was  
 311 evaluated by the Concordance Correlation Coefficient,  $\rho_L$  :

$$\rho_L = \frac{2s_{xy}}{z_x^2 + z_y^2 + (m_x - m_y)^2} \quad (5)$$

312 where  $m_x$ ,  $m_y$ ,  $s_x$ ,  $s_y$ ,  $s_{xy}$  are means, standard deviations and covariances of the two data series  
 313 ( $x = \sigma_{b,EMI}$ ;  $y = \sigma_{b,TDR}$ ), respectively.

314 Scatter plots of the  $\sigma_{b,EMI}$  and  $\sigma_{b,TDR}$  data series (both original and filtered) were evaluated by  
 315 the line of perfect concordance (1:1 line) and the reduced major axis of the data (RMA)  
 316 (Freedman et al., 1991). The method combines measurements of both precision and accuracy  
 317 to determine how close the two data series are to the line of perfect concordance  $\sigma_{b,EMI} = \sigma_{b,TDR}$ .

318 Compared to the classical Pearson correlation coefficient,  $\rho_P$ :

$$\rho_P = \frac{s_{xy}}{s_x s_y}, \quad (6)$$

319  $\rho_L$  not only measures the strength of linear relationship (how close the data in the scatter plot  
 320 are to a line), but also the level of agreement (how close that line is to the line of perfect  
 321 agreement, the 1:1 line). In this sense,  $\rho_L$  may also be calculated as (Cox, 2006):

$$\rho_L = \rho_P C_b, \quad (7)$$

$$C_b = \frac{2}{(v+1/v+u^2)},$$

$$v = s_x / s_y,$$

322 and

$$u = (m_x - m_y) / \sqrt{s_x s_y},$$

323 where  $C_b$  is the bias correction factor measuring how far the best-fit line deviates from the 1:1  
 324 line. The maximum value of  $C_b = 1$  ( $0 < C_b < 1$ ) corresponds to no deviation from the line. The  
 325 smaller  $C_b$  is, the greater the deviation from the line. In other words,  $C_b$  is a measure of  
 326 accuracy (how much the average estimate differs from the average measurement value,  
 327 assumed to be the true value) and refers to the systematic error, whereas  $\rho_P$  is a measure of  
 328 precision (measures the variability of measurements around their own average) and refers to  
 329 the random error. The RMA line is given by:

$$y = (m_y - \beta m_x) + \beta x = \alpha + \beta x. \quad (8)$$

330 This line passes through the means of the x and y values and has slope given by the sign of  
 331 Pearson's correlation coefficient,  $\rho_P$ , and the ratio of the standard deviations,  $s$ , of the two  
 332 series (Freedman et al., 1991; Corwin and Lesch, 2005):

$$\beta = s_y / s_x. \quad (9)$$

333  $\rho_L$  increases in value as (i) the RMA approaches the line of perfect concordance (a matter of  
 334 accuracy) and (ii) the data approach the RMA (a matter of precision). In the ideal case of  
 335 perfect concordance, the intercept of the RMA,  $\alpha$ , should be 0 and  $\beta$  should be 1. Therefore,  $\alpha$   
 336  $\neq 0$  or  $\beta \neq 1$  indicate additive and/or multiplicative biases (location and/or scale shifts). The  
 337 concordance was evaluated for the original TDR data, as well as for the filtered TDR data. For  
 338 the analysis described in detail later in the paper, it is worth noting that the coefficients  $\alpha$  and  $\beta$

339 depend only on the statistical characteristics (mean and standard deviation) of the two series,  
340 as  $\alpha = m_y - \beta m_x$  and  $\beta = s_y / s_x$ .

341

#### 342 *Fourier filtering*

343 Because of their relatively small observation volume ( $\sim 10^{-3} \text{ m}^3$ ), TDR sensors provide quasi-  
344 pointlike measurements and are, thus, more effective in capturing small-scale variability (in  
345 water content, solute concentrations) induced by natural soil heterogeneity. Thus, the  
346 variability within a set of TDR readings is expected to originate from a combination of small and  
347 large-scale heterogeneities (high and low spatial frequency components). By contrast, the EMI  
348 measurements (because of the size and physics of the instrumentation) necessarily integrate  
349 out the small-scale variability at the TDR scale of investigation.

350 Hence, in order to make the two datasets comparable, the original spatial TDR data series need  
351 to be filtered to remove the variation from small-scale heterogeneities (recorded only by the  
352 TDR probe). In this way, only the information at a spatial scale equal to or larger than the  
353 observation volume of both sensors is preserved.

354 Thus, a simple filter based on the Fourier Transform (FT) is applied to the TDR series. So, a low-  
355 pass frequency filtering is performed on the TDR data to remove ~~all—components~~all  
356 components related to the ~~small-scales~~small-scale heterogeneities and make it comparable with  
357 the EMI measurements. More specifically, for each transect, we consider the  $\sigma_{b,EMI}$   
358 reconstruction and, for each of its 1D models, calculate the average conductivity value within  
359 each depth interval for which the TDR data are available (namely: 0.0-0.2 m, 0.2-0.4 m, 0.4-0.6  
360 m). Hence, for each depth interval, along the entire transect, we can calculate the mean and  
361 standard deviation of the conductivity values retrieved from the EMI observations.

362 Subsequently, this standard deviation (associated with the EMI data) is compared with the  
363 standard deviation of the iteratively low-pass filtered TDR data for the same depth interval. In  
364 this way, an optimal cut-off frequency can be selected to make the scales of the two kinds of  
365 measurements compatible. Figure 6 shows the comparison between the standard deviations of  
366 the EMI and filtered TDR data, for the 50-6dS transect, at 0.2-0.4 m depth. In this specific case,  
367 the selected cut-off frequency to filter the TDR data is 0.313 cycles/m, corresponding to a 3.2 m  
368 range. This is not surprising at this is of the order of magnitude of the footprint of the EMI  
369 measurements.

370

## 371 **Results and Discussion**

372 Hereafter, the original and filtered data will be respectively labeled ORG and FLT. The graphs on  
373 the top panels in Fig. 7 compare  $\sigma_{b,TDR}$  measured by TDR against the corresponding conductivity  
374  $\sigma_{b,EMI}$  retrieved by the EMI (sharp) inversion for the all the transects. From the left, the graphs  
375 refer respectively to the transects identified as 100-6dS, 50-6dS, 100-1dS and 50-1dS. All plots  
376 show the data for the entire investigated profile between 0.0 and 0.6 m, together with the line  
377 of perfect concordance (1:1, black line), and the main regression axis (MRA, red line).

378 The general conclusion is that, in all four transects, and for all three considered depth-layers,  
379 the  $\sigma_{b,EMI}$  values underestimate the  $\sigma_{b,TDR}$  measurements, such that the MRA line generally lies  
380 above the 1:1 line. Not surprisingly, the EMI result seems quite insensitive to TDR variability.  
381 Also, a considerable scatter around the MRA line may be observed for all transects.

382 Table 1 shows the MRA coefficients ( $C_b$ ,  ~~$\alpha$~~ ,  $\beta$ ), as well as the Pearson,  $\rho_p$ , and the  
383 concordance correlation,  $\rho_L$ , for the three depth-layers and for all four transects investigated.

384 We recall that the bias correction factor  $C_b$ , the slope  $\beta$ , and the intercept  $\alpha$  should be  
385 respectively close to 1, 1 and 0, for the MRA to approximate the line of perfect concordance.

386 For all the transects and all the depth-layers considered, the parameters confirm the relatively  
387 loose relationship between  $\sigma_{b,EMI}$  and  $\sigma_{b,TDR}$  already observed in the graphs, both in terms of  
388 accuracy (the distance of the MRA line from the 1:1) and precision (the data scatter around the  
389 MRA line).

390 Von Hebel et al. (2014) found a similar behavior when comparing their EMI and ERT datasets. In  
391 that case, the  $EC_a$  values measured by EMI systematically underestimated the  $EC_a$  generated by  
392 applying EMI forward modeling to the  $\sigma_b$  distribution retrieved by ERT. To remove the bias, the  
393 authors performed a linear regression between measured and predicted  $EC_a$  after applying a  
394 ten-term moving average to the original data. By using the regression coefficients, all the  
395 measured  $EC_a$  values were converted to ERT-calibrated  $EC_a$  values.

396 Here, we follow a different approach to calibrate the  $\sigma_{b,EMI}$  values against the  $\sigma_{b,TDR}$   
397 measurements based on the MRA coefficients and, so, on the statistical parameters (mean and  
398 standard deviation) of the two data series. Specifically, the present approach looks for a  
399 systematic correction of the bias based on well-defined statistical sources of the discrepancies.  
400 In short, the proposed method performs the calibration in the  $\sigma_b$  model-space, instead of the  
401  $EC_a$  data-space. Our model-space approach mostly relies on the statistical parameters of the  
402 two series. Analyzing the role of these statistics in explaining the discrepancies between EMI  
403 and TDR data observed in Fig. 7a may help to understand how they can be effectively used for  
404 making EMI results directly comparable with the TDR values.

405 In nearly all of the graphs in the top panels in Fig. 7, the discrepancies between  $\sigma_{b,EMI}$  and  $\sigma_{b,TDR}$   
406 values can be decomposed in the following components:

407 1. The distance along the  $\sigma_{b,EMI}$  axis of the MRA line from the 1:1 line, that is the difference  
408 between the  $\sigma_{b,EMI}$  and the  $\sigma_{b,TDR}$  means.

409 2. The difference in the slope of the MRA and of the 1:1 lines, which stems from the different  
410 variability of  $\sigma_{b,EMI}$  (its standard deviation) and that of  $\sigma_{b,TDR}$ . We recall here that the slope of  
411 the MRA is just the ratio of the two standard deviations,  $\hat{\beta} = s_y / s_x$ .

412 3. The scatter of the data around the MRA line, which may come from different sensors' noise  
413 and the influence of surrounding conditions (e.g., temperature).

414 Below, we analyze in detail the role of all these three points with the support of the measured  
415 data.

416 1. The distance of the MRA from the 1:1 line is mostly due to the difference in the observed  
417 means. The plot in Figure 8a compares the means for the two original series (squares-solid line  
418 for TDR, circles-dashed line for EMI). Figure 8b reports the same comparison on a 1:1 plot  
419 (triangles-solid regression line). The mean values confirm the general underestimation of TDR  
420 by the EMI data. However, the trends are evidently similar, which is reflected in the high  
421 correlation between the means of the two series, with a significantly high  $R^2=0.81$ . This high  
422 correlation has very positive implications from an applicative point of view, since, after the  
423 calibration in a specific site, it allows the EMI mean to be inferred given the mean of TDR  
424 readings taken in that soil, and thus provides the possibility to migrate the more reliable TDR  
425 information across the larger area that can be practically investigated during an EMI survey.

426 2. The different slope of the two lines has to be ascribed to the different variability of the two  
427 series. Figure 9a compares the standard deviations for the two original series (squares-solid line  
428 for TDR, circles-dashed line for EMI). Figure 9b reports the same comparison on a 1:1 plot  
429 (triangles-solid regression line). Conceptually, the different variability of the two series can be  
430 related to the different sensor observation volumes (originated from the different spatial  
431 sensitivity of the sensors - Coppola et al. 2016). For TDR probes, most of the measurement

432 sensitivity is close to the rods (Ferré et al. 1998b). Conversely, the spatial resolution of inverted  
433 EMI  $EC_a$  values may be much lower as the resolution of the EMI result depends on the physics  
434 of the method, the specifications (and configuration) of the recording device, and the  
435 regularization strategy applied during the inversion. Thus, the EMI is generally unable to  
436 capture the small-scale variability seen by the TDR. For our calibration purposes, it is important  
437 to make the variability of EMI and TDR conductivities actually comparable. As discussed by  
438 Coppola et al., (2016), a possible method can consist in filtering out the high frequency  
439 components (at small spatial scale) of the original TDR data, while retaining the lower  
440 frequency information. This corresponds to keep the information at a spatial scale larger than  
441 the observation volume of the TDR sensor and attuned with the resolution of the  $\sigma_{b,EMI}$   
442 distribution. From a practical point of view, this makes sense, as TDR readings are often “too  
443 local” to actually represent the macroscopic physical characteristics of interest for applications  
444 (water content, solute concentrations). The volume explored by a TDR probe may, or may not,  
445 include preferential channels (Mallants et al., 1994; Oberdörster et al., 2010), stones (Coppola  
446 et al., 2011; Coppola et al., 2013), small-scale changes in the texture and structure (Coppola et  
447 al., 2011), which can make the interpretation of local measurements difficult for practical  
448 applications. In this sense, EMI’s removal of these small-scale effects may be desirable from a  
449 management perspective. Consistently, the original TDR data are conditioned via a low-pass  
450 filtering, as described in the Data Handling section. The filtering results, in terms of standard  
451 deviations, are reported in Fig. 9a (crosses-dashed line) and Fig. 9b (squares-dashed regression  
452 line). As expected, the low-pass filter makes the standard deviations much closer (almost  
453 overlapping) in all transects and all considered depth-layers. The regression improved  
454 significantly from 0.25 for the original data to 0.78 after the TDR data filtering.

455 3. The scatter is consistently reduced by the spatial filtering (as similarly discussed in Von Hebel  
456 et al., 2014).

457

458 Eventually, the calibrated  $\sigma_{b,EMI}^{rg}$  distribution (superscript *rg* means: EMI data after regression)

459 can then be obtained from the original  $\sigma_{b,EMI}$  via the linear mapping:

$$460 \quad \sigma_{b,EMI}^{rg} = \alpha + \beta \sigma_{b,EMI} , \quad (10)$$

461 where the coefficients  $\alpha$  and  $\beta$  can be easily calculated from the means and standard  
462 deviations of the EMI results and the filtered TDR data. Thus, if  $m_{EMI}$  and  $m_{TDR(FLT)}$ , and  $s_{EMI}$  and  
463  $s_{TDR(FLT)}$  are, respectively, the means and the standard deviations of the original  $\sigma_{b,EMI}$  EMI data  
464 and of the filtered  $\sigma_{b,TDR(FLT)}$  TDR data, the MRA line coefficients can be expressed as

$$465 \quad \alpha = m_{TDR(FLT)} - \beta m_{EMI} \quad \text{and} \quad \beta = s_{TDR(FLT)} / s_{EMI} .$$

466 The bottom panels in Fig. 7 show the results of the application of the linear mapping. In  
467 particular, they compare the calibrated EMI data (EMI *rg*) with the filtered TDR (TDR *FLT*)  
468 measurements. The MRA parameters and the concordance coefficients in the case of filtered  
469 TDR data are reported in Table 2. Clearly, considering the (calibrated) EMI and (filtered) TDR  
470 standard deviations turns the MRA line to be practically matching the 1:1 line, with the  
471 coefficient  $\beta$  approaching to 1. Moreover, from Table 2, the improvement of the bias  $C_b$  and the  
472 concordance  $\rho_L$  is generally significant. On the other hand, the Pearson's correlation  $\rho_P$  is not  
473 influenced by the recalibration as the proposed approach deals with the statistics of the data  
474 series rather than the single data. Thus, after the application of the low-pass filter to the TDR  
475 data, the coefficient  $\beta$  is close to 1, and the calibration turns out to be (almost) a simple shift of  
476 the inverted  $\sigma_{b,EMI}$ . The amount of this shift is equal to the difference between the mean values  
477  $m_{TDR(FLT)}$  and  $m_{EMI}$ . To summarize, the TDR filtering allows removing the outlier values generated

478 by the small scale variability and preserving the information content necessary to properly  
479 calculate the shift required for the absolute calibration of the EMI inversion results.

480 Figure 10 shows, on the left, the original  $\sigma_{b,EMI}$  distribution to be compared against the  $\sigma_{b,EMI}^{rg}$   
481 results (on the right) obtained through the application of the linear transformation in Eq. 10.  
482 The calibrated transects preserves the spatial variability of the original EMI inversions, but are  
483 now characterized by value ranges that are more realistic (as they are obviously closer to the  
484 TDR measurements assumed to be more representative of the real soil conditions). The results  
485 in Fig. 10 obviously reflect the experimental irrigation set-up. Hence, not surprisingly, the  
486 conductivity of the 100-6dS case (irrigated with 100% of the water at 6 dSm<sup>-1</sup>) is the most  
487 effected (Fig. 10d), while the 50-1dS case (corresponding to an irrigation with 50% of the water  
488 at 1 dSm<sup>-1</sup>) is the example with the lowest conductivity range (Fig. 10g). The intermediate  
489 irrigation tests 50-6dS (Fig. 10e) and 100-1dS (Fig. 10f) show very similar maximum and  
490 minimum conductivity values over the two transects. However, there is a difference concerning  
491 the spatial distributions. In particular, in the 100-1dS case, the highest  $\sigma_{b,EMI}^{rg}$  values  
492 characterize not only the shallower 0.0 - 0.1 m portion (Fig. 10f), but they appear to spread  
493 almost homogenously all over the section. On the contrary, in the 50-6dS test, the maximum  
494 values are limited to the first soundings at the beginning of the transect and to the 0.2 - 0.4 m  
495 depth interval. More important, if we compare the original 50-6dS (Fig. 10b) and 100-1dS (Fig.  
496 10c) conductivity distributions against the corresponding calibrated results (Fig. 10e and Fig.  
497 10f), the original  $\sigma_{b,EMI}$  section, which used to be the generally most conductive one (50-6dS,  
498 Fig. 10b), is now the most resistive (Fig. 10e) and vice versa. This, one more time, demonstrates  
499 that the proper calibration may lead to significantly different conclusions.

500

501 As already discussed, the high correlation of the means and the standard deviations of the two  
502 series are central for this procedure to be of practical interest. In short, the procedure can be  
503 summarized as follows: (i) An area is monitored via EMI survey and a few TDR calibration  
504 measurements are collected concurrently. (ii) The availability of the two different datasets  
505 allows performing the regression for the mean and the standard deviation of the original EMI  
506 inversion results and the filtered TDR data, like those shown in Fig.s 8b and 9b. (iv) These  
507 statistical parameters can be promptly used for the calculation of the coefficients  $\alpha$  and  $\beta$  to be  
508 inserted into Eq. 10. (v) The original EMI inversion results are not always reliable when  
509 compared with the direct measurements obtained by using a TDR probe. Rather, they only  
510 contain the low-frequency information supplied by TDR (most likely, together with some shifts  
511 connected with the poor absolute calibration of the EMI system and/or the working conditions,  
512 e.g., the temperature). Thus, for quantitative analyses, it may be crucial to transform the  
513 original EMI result  $\sigma_{b,EMI}$  into a new, calibrated section  $\sigma_{b,EMI}^{rg}$  by means of the linear mapping  
514 in Eq. 10.

515 The proposed workflow enables us to translate the original non-calibrated  $\sigma_{b,EMI}$  data into the  
516 actual  $\sigma_b$  we would collect in ideal conditions, and which would perfectly match “low-  
517 resolution” TRD measurements.  $\sigma_{b,EMI}^{rg}$  is our best possible estimation of the true electrical  
518 conductivity at the scale of investigation of the EMI survey: it is the original  $\sigma_{b,EMI}$  after the  
519 application of the appropriate rescaling and shifts deduced by the more reliable and absolutely  
520 calibrated TDR measurements.

521

522 **Conclusions**

523 The objective of the paper is to infer the bulk electrical conductivity distribution in the root  
524 zone from multi-height (potentially non-calibrated) EMI readings. TDR direct measurements are  
525 used as ground-truth  $\sigma_b$  data to evaluate the correctness of the  $\sigma_b$  estimations generated by  
526 EMI inversion. For all four transects and for all three depth-layers considered in this study, the  
527  $\sigma_{b,EMI}$  values underestimate the  $\sigma_{b,TDR}$  measurements, such that the MRA line generally lies  
528 above the 1:1 line. Also, a considerable scatter around the MRA line was observed for all  
529 transects.

530 The proposed analysis allows discussing the physical reasons for the differences between EMI-  
531 and TDR-based electrical conductivity and developing an approach to calibrate the original  
532  $\sigma_{b,EMI}$  by using the  $\sigma_{b,TDR}$  measurements. Our approach is based on the MRA coefficients and,  
533 hence, on the statistical parameters (mean and standard deviation) of the two series.  
534 Specifically, the approach looks for a systematic correction of the bias based on well-defined  
535 statistical sources of the discrepancies. A low-pass filtering has been carried out on the TDR  
536 data to obtain a significantly high correlation between the standard deviations of the two data  
537 series. After that, a simple linear transformation can be applied to the originally inverted EMI  
538 section  $\sigma_{b,EMI}$  to get a calibrated  $\sigma_b$  result.

539 The proposed strategy lies on the assumption that TDR direct measurements supply absolutely  
540 calibrated observations of the electrical conductivity of the soil and can be effectively used to  
541 calibrate the conductivity distributions inferred from EMI data. The availability of EMI  
542 calibrated data paves the way to reliable reconstructions of the electrical conductivity  
543 distribution over large areas (typical for EMI surveys, but not for TDR campaigns) unaffected by  
544 the usual EMI miscalibrations. This, in turn, can result in the possibility of effective time-lapse  
545 surveys and/or in consistent merging of subsequent surveys.

546 On the other hand, the proposed statistical workflow for making the TDR measurement  
547 comparable with the associated EMI results provides a more sophisticated approach than  
548 simple smoothing to upscale the TDR data. Thus, from the opposite perspective, the approach  
549 in question can be used to tackle the problems connected with handling the TDR data  
550 characterized by excessively high spatial resolution.

551

552

553

#### 554 **References**

555 Abdu, H., D.A. Robinson, and S.B. Jones. 2007. Comparing bulk soil electrical conductivity  
556 determination using the DUALEM-1S and EM38-DD electromagnetic induction instruments. *Soil*  
557 *Sci. Soc. Am. J.* 71 (1):189-196. doi: 10.2136/sssaj2005.0394.

558

559 Amezketa, E. 2006. An integrated methodology for assessing soil salinization, a pre-condition  
560 for land desertification. *J. Arid Environ.* 67 (4):594-606. doi: 10.1016/j.jaridenv.2006.03.010.

561

562 Beard, L. P, and J. E. Nyquist. 1998. Simultaneous inversion of airborne electromagnetic data  
563 for resistivity and magnetic permeability. *Geophysics* 63 (5): P1556-1564.

564

565 Bechtold, M., J.A. Huisman, L. Weihermüller, and H. Vereecken. 2010. Accurate  
566 determination of the bulk electrical conductivity with the TDR100 cable tester. *Soil Sci. Soc.*  
567 *Am. J.* 74, 495–501

568

569 Borchers, B., T. Uram, and J.M.H. Hendrickx. 1997. Tikhonov regularization of electrical  
570 conductivity depth profiles in field soils. *Soil Sci. Soc. Am. J.* 61 (4):1004-1009. doi:  
571 10.2136/sssaj1997.03615995006100040002x.  
572

573 Cassiani, G., N. Ursino, R. Deiana, G. Vignoli, J. Boaga, M. Rossi, M. T. Perri, M. Blaschek, R.  
574 Duttmann, S. Meyer, R. Ludwig, A. Saddu, P. Dietrich, and U. Werban. *Vadose Zone J.*  
575 doi:10.2136/vzj2011.0195  
576

577 Coppola, A., G. Dragonetti, A. Comegna, N. Lamaddalena, B. Caushi, M.A. Haikal, and A. Basile.  
578 2013. Measuring and modeling water content in stony soils. *Soil Till. Res.* 128:9-22.  
579

580 Coppola, A., K. Smettem, A. Ajeel, A. Saeed, G. Dragonetti, A. Comegna, N. Lamaddalena, and A.  
581 Vacca. 2016. Calibration of an electromagnetic induction sensor with time-domain  
582 reflectometry data to monitor rootzone electrical conductivity under saline water irrigation.  
583 *Eur. J. of Soil Sci.* 67 (6):737-748. doi: 10.1111/ejss.12390.  
584

585 Coppola, A., N. Chaali, G. Dragonetti, N. Lamaddalena, and A. Comegna. 2015. Root uptake  
586 under non-uniform root-zone salinity. *Ecohydrology.* 8 (7):1363-1379. doi: 10.1002/eco.1594.  
587

588 Coppola, A., A. Comegna, G. Dragonetti, M. Dyck, A. Basile, N. Lamaddalena, M. Kassab, and V.  
589 Comegna. 2011. Solute transport scales in an unsaturated stony soil. *Adv. Water Resour.* 34  
590 (6):747-759. doi: <http://dx.doi.org/10.1016/j.advwatres.2011.03.006>.  
591

592 Corwin, D.L., and S.M. Lesch. 2005. Apparent soil electrical conductivity measurements in  
593 agriculture. *Comput. Electron. Agr.* 46 (1):11-43.  
594

595 Cox, N.J. 2006. Assessing agreement of measurements and predictions in geomorphology.  
596 *Geomorphology.* 76 (3):332-346.  
597

598 Dalton, F. N., W. N. Herkelrath, D. S. Rawlins, and J. D. Rhoades. 1984. Time domain  
599 reflectometry: Simultaneous measurement of soil water content and electrical conductivity  
600 with a single probe. *Science* 224, 989–990.  
601

602 Deidda, G.P., E. Bonomi, and C. Manzi. 2003. Inversion of electrical conductivity data with  
603 Tikhonov regularization approach: some considerations. *Ann. Geophys.*  
604

605 Deidda, G.P., C. Fenu, and G. Rodriguez. 2014. Regularized solution of a nonlinear problem in  
606 electromagnetic sounding *Inverse Probl.* 30 (12):125014.  
607

608 Deidda, G.P., P. Diaz De Alba, and G. Rodriguez. 2017. Identifying the magnetic permeability in  
609 multi-frequency EM data inversion. *Submitted.*  
610

611 Díaz de Alba, P., and G. Rodriguez. 2016. Regularized Inversion of Multi-Frequency EM Data in  
612 Geophysical Applications. In *Trends in Differential Equations and Applications*, 357-369.  
613 Springer.  
614

615 Doolittle, J.A., and E.C. Brevik. 2014. The use of electromagnetic induction techniques in soils  
616 studies. *Geoderma* . 223:33-45.  
617

618 Farquharson, C. G., Oldenburg, D. W., and Routh, P. S. 2003. Simultaneous 1D inversion of loop-  
619 loop electromagnetic data for both magnetic susceptibility and electrical conductivity.  
620 *Geophysics*. 68, 1857–1869.  
621

622 Ferré, P.A., J. D. Redman, D.L. Rudolph, and R.G. Kachanoski. 1998a. The dependence of the  
623 electrical conductivity measured by time domain reflectometry on the water content of a sand.  
624 *Water Resour. Res.* 34 (5):1207-1213  
625

626 Ferré, P.A., J.H. Knight, D.L. Rudolph, and R.G. Kachanoski. 1998b. The sample areas of  
627 conventional and alternative time domain reflectometry probes. *Water Resour. Res.* 34  
628 (11):2971-2979.  
629

630 Fiandaca, G., J. Doetsch, G. Vignoli, and E. Auken. 2015. Generalized focusing of time-lapse  
631 changes with applications to direct current and time-domain induced polarization inversions.  
632 *Geophys. J. Int.* 203 (2):1101-1112. doi: 10.1093/gji/ggv350.  
633

634 Freedman, D., R. Pisani, R. Purves, and A. Adhikari. 1991. *Statistics* (2nd ed.). New York: W. W.  
635 Norton.  
636

637 Gebbers, R., E. Lück, M. Dabas, and H. Domsch. 2009. Comparison of instruments for  
638 geoelectrical soil mapping at the field scale. *Near Surf. Geophys.* 7 (3):179-190. doi:  
639 10.3997/1873-0604.2009011

640

641 [Guillemoteau, J., F. X. Simon, E. Luck, and J. Tronicke, 2016, 1D sequential inversion of portable](#)  
642 [multi-configuration electromagnetic induction data: \*Near Surface Geophysics\*,14, 411-420.](#)

643

644 Günther, T. 2011. Timelapse ERT inversion approaches and their applications. *Geoelectric*  
645 *Monitoring*:91.

646

647 Heimovaara, T.J., A.G. Focke, W. Bouten, and J.M. Verstraten. 1995. Assessing temporal  
648 variations in soil water composition with time domain reflectometry. *Soil Sci. Soc. Am. J.* 59  
649 (3):689-698. doi: 10.2136/sssaj1995.03615995005900030009x.

650

651 Hendrickx, J.M.H., B. Borchers, D.L. Corwin, S.M. Lesch, A.C. Hilgendorf, and J. Schlue. 2002.  
652 Inversion of soil conductivity profiles from electromagnetic induction measurements. *Soil Sci.*  
653 *Soc. Am. J.* 66 (3):673-685. doi: 10.2136/sssaj2002.6730.

654

655 Huisman, J.A., C. P. Lin, L. Weihermüller, H. Vereecken. 2008. Accuracy of Bulk Electrical  
656 Conductivity Measurements with Time Domain Reflectometry. *Vadose Zone J.* 7, 426–433

657

658 Koestel, J., A. Kemna, M. Javaux, A. Binley, H. Vereecken. 2008. Quantitative imaging of solute  
659 transport in an unsaturated and undisturbed soil monolith with 3-D ERT and TDR. *Water*  
660 *Resour. Res.* 44, W12411, doi:10.1029/2007WR006755.

661

662 Lavoué, F., J. van der Kruk, J. Rings, F. André, D. Moghadas, J.A. Huisman, S. Lambot, L.

663 Weihermüller, J. Vanderborght, and H. Vereecken. 2010. Electromagnetic induction calibration

664 using apparent electrical conductivity modelling based on electrical resistivity tomography.

665 *Near Surf. Geophys.* 8 (6):553-561.

666

667 Lesch, S.M., J.D. Rhoades, L.J. Lund, and D.L. Corwin. 1992. Mapping soil salinity using

668 calibrated electromagnetic measurements. *Soil Sci. Soc. Am. J.* 56 (2):540-548. doi:

669 10.2136/sssaj1992.03615995005600020031x.

670

671 Ley-Cooper, A.Y., A. Viezzoli, J. Guillemoteau, G. Vignoli, J. Macnae, L. Cox, and T. Munday.

672 2015. Airborne electromagnetic modelling options and their consequences in target definition.

673 *Explor. Geophys.* 46 (1):74-84. doi: 10.1071/eg14045.

674

675 Lin, K. 1989. A concordance correlation coefficient to evaluate reproducibility. *Biometrics*:255-

676 268.

677

678 Lin, C.P., C. C. Chung, J. A. Huisman, and S. H. Tang. 2008. Clarification and calibration of

679 reflection coefficient for time domain reflectometry electrical conductivity measurement. *Soil*

680 *Sci. Soc. Am. J.* 72, 1033-104072.

681

682 Lin, C.P., C. C. Chung, and S. H. Tang. 2007. Accurate time domain reflectometry measurement

683 of electrical conductivity accounting for cable resistance and recording time. *Soil Sci. Soc. Am. J.*

684 71,1278–1287.

685

686 Mallants, D., M. Vanclooster, M. Meddahi, and J. Feyen. 1994. Estimating solute transport in  
687 undisturbed soil columns using time-domain reflectometry. *Journal Contam. Hydrol.* 17 (2):91-  
688 109. doi: 10.1016/0169-7722(94)90016-7.

689

690 McNeill, J.D. 1980. Electromagnetic terrain conductivity measurement at low induction  
691 numbers. Geonics Limited Ontario, Canada.

692

693 Mester, A., J. Van Der Kruk, E. Zimmermann, and H. Vereecken. 2011. Quantitative Two-Layer  
694 Conductivity Inversion of Multi-Configuration Electromagnetic Induction Measurements.  
695 *Vadose Zone J.* 10:1319-1330. doi: 10.2136/vzj2011.0035.

696

697 Minsley, B.J., B.D. Smith, R. Hammack, J.I. Sams, and G. Veloski. 2012. Calibration and filtering  
698 strategies for frequency domain electromagnetic data. *J. Appl. Geophys.* 80:56-66. doi:  
699 10.1016/j.jappgeo.2012.01.008.

700

701 Moghadas, D., F. André, J.H. Bradford, J. van der Kruk, H. Vereecken, and S. Lambot. 2012.  
702 Electromagnetic induction antenna modelling using a linear system of complex antenna  
703 transfer functions. *Near Surf. Geophys.* 10 (3):237-247. doi: 10.3997/1873-0604.2012002

704

705 Noborio, K. 2001. Measurement of soil water content and electrical conductivity by time  
706 domain reflectometry: A review. *Comput. Electron. Agric.* 31:213–237.

707

708 [Noh, K., K. H. Lee, S. Oh, S. J. Seol, and J. Byun, 2017, Numerical evaluation of active source](#)  
709 [magnetics as a method for imaging high-resolution near-surface magnetic heterogeneity:](#)  
710 [Geophysics, 82, J27-J38.](#)  
711  
712 Nüsch, A.K., P. Dietrich, U. Werban, T. Behrens, and N. Prakongkep. 2010. Acquisition and  
713 reliability of geophysical data in soil science. Paper read at 19th world congress of soil science,  
714 soil solutions for a changing world, Brisbane, Australia.  
715  
716 Oberdörster, C., J. Vanderborght, A. Kemna, and H. Vereecken. 2010. Investigating preferential  
717 flow processes in a forest soil using time domain reflectometry and electrical resistivity  
718 tomography. *Vadose Zone J.* 9 (2):350-361.  
719  
720 Pagliara, G., and G. Vignoli. 2006. Focusing inversion techniques applied to electrical resistance  
721 tomography in an experimental tank. In *XI International Congress of the International*  
722 *Association for Mathematical Geology.*  
723  
724 Rhoades, J.D., and D.L. Corwin. 1981. Determining soil electrical conductivity-depth relations  
725 using an inductive electromagnetic soil conductivity meter. *Soil Sci. Soc. Am. J.* 45 (2):255-260.  
726  
727 Rhoades, J.D., and J. van Schilfgaarde. 1976. An electrical conductivity probe for determining  
728 soil salinity. *Soil Sci. Soc. Am. J.* 40 (5):647-651. doi:  
729 10.2136/sssaj1976.03615995004000050016x.  
730

731 Robinson, D.A., and S.P. Friedman. 2003. A method for measuring the solid particle permittivity  
732 or electrical conductivity of rocks, sediments, and granular materials. *J. Geophys. Res-Sol Ea*.  
733 108 (B2):2076. doi: 10.1029/2001JB000691.

734

735 Robinson, D. A., S. B. Jones, J. M. Wraith, D. Or, and S. P., Friedman. 2003. A review of  
736 advances in dielectric and electrical conductivity measurement using time domain  
737 reflectometry. *Vadose Zone J.* 2, 444–475.

738

739 Robinson, D.A., I. Lebron, S.M. Lesch, and P. Shouse. 2004. Minimizing Drift in Electrical  
740 Conductivity Measurements in High Temperature Environments using the EM-38. *Soil Sci. Soc.*  
741 *Am. J.* 68 (2):339-345. doi: 10.2136/sssaj2004.3390.

742

743 Robinson, D.A., H. Abdu, I. Lebron, and S.B. Jones. 2012. Imaging of hill-slope soil moisture  
744 wetting patterns in a semi-arid oak savanna catchment using time-lapse electromagnetic  
745 induction. *J. Hydrol.* 416–417:39-49. doi:https://doi.org/10.1016/j.jhydrol.2011.11.034.

746

747 Santos, F.A. Monteiro, J. Triantafilis, K.E. Bruzgulis, and J.A.E. Roe. 2010. Inversion of  
748 Multiconfiguration Electromagnetic (DUALEM-421) Profiling Data Using a One-Dimensional  
749 Laterally Constrained Algorithm. *Vadose Zone J.* 9:117-125. doi: 10.2136/vzj2009.0088.

750

751 [Sasaki, Y., J. Kim, and S. Cho, 2010, Multidimensional inversion of loop-loop frequency domain](#)  
752 [EM data for resistivity and magnetic susceptibility: \*Geophysics\*, 75, 213-223.](#)

753

754 Sheets, K.R., and J.M.H. Hendrickx. 1995. Noninvasive soil water content measurement using  
755 electromagnetic induction. *Water Resour. Res.* 31 (10):2401-2409.  
756  
757 Shumway, R.H. 1988. *Applied Time Series Analysis*: Prentice-Hall, Englewood Cliffs, NJ.  
758  
759 Sudduth, K.A., S.T. Drummond, and N.R. Kitchen. 2001. Accuracy issues in electromagnetic  
760 induction sensing of soil electrical conductivity for precision agriculture. *Comput. Electron. Agr.*  
761 31 (3):239-264. doi: 10.1016/S0168-1699(00)00185-X.  
762  
763 Thomsen, A., K. Schelde, P. Drøschler, F. Steffensen. 2007. Mobile TDR for geo-referenced  
764 measurement of soil water content and electrical conductivity. *Precision Agriculture* 8, 213–223  
765  
766 Topp, G. C., M. Yanuka, W. D. Zebchuk, and S. Zegelin. 1988. Determination of electrical  
767 conductivity using time domain Reflectometry: Soil and water experiments in coaxial lines.  
768 *Water Resour. Res.* 24, 945–952.  
769  
770 Triantafilis, J., G.M. Laslett, and A.B. McBratney. 2000. Calibrating an electromagnetic induction  
771 instrument to measure salinity in soil under irrigated cotton. *Soil Sci. Soc. Am. J.* 64 (3):1009-  
772 1017. doi: 10.2136/sssaj2000.6431009x.  
773  
774 Ursino, N., G. Cassiani, R. Deiana, G. Vignoli and J. Boaga. 2014. Measuring and modeling water-  
775 related soil–vegetation feedbacks in a fallow plot. *Hydrol. Earth Syst. Sci.* 18, 1105–1118.  
776

777 Vignoli, G., G. Fiandaca, A.V. Christiansen, C. Kirkegaard, and E. Auken. 2015. Sharp spatially  
778 constrained inversion with applications to transient electromagnetic data. *Geophys. Prospect.*  
779 63 (1):243-255.  
780

781 Vignoli, G., V. Sapia, A. Menghini, and A. Viezzoli. 2017. Examples of Improved Inversion of  
782 Different Airborne Electromagnetic Datasets Via Sharp Regularization. *J. Environ. Eng. Geophys.*  
783 22 (1):51-61. doi: 10.2113/jeeeg22.1.51.  
784

785 Vignoli, G., R. Deiana, and G. Cassiani. 2012. Focused inversion of vertical radar profile (VRP)  
786 traveltime data. *Geophysics*. 77 (1):H9-H18. doi: 10.1190/geo2011-0147.1.  
787

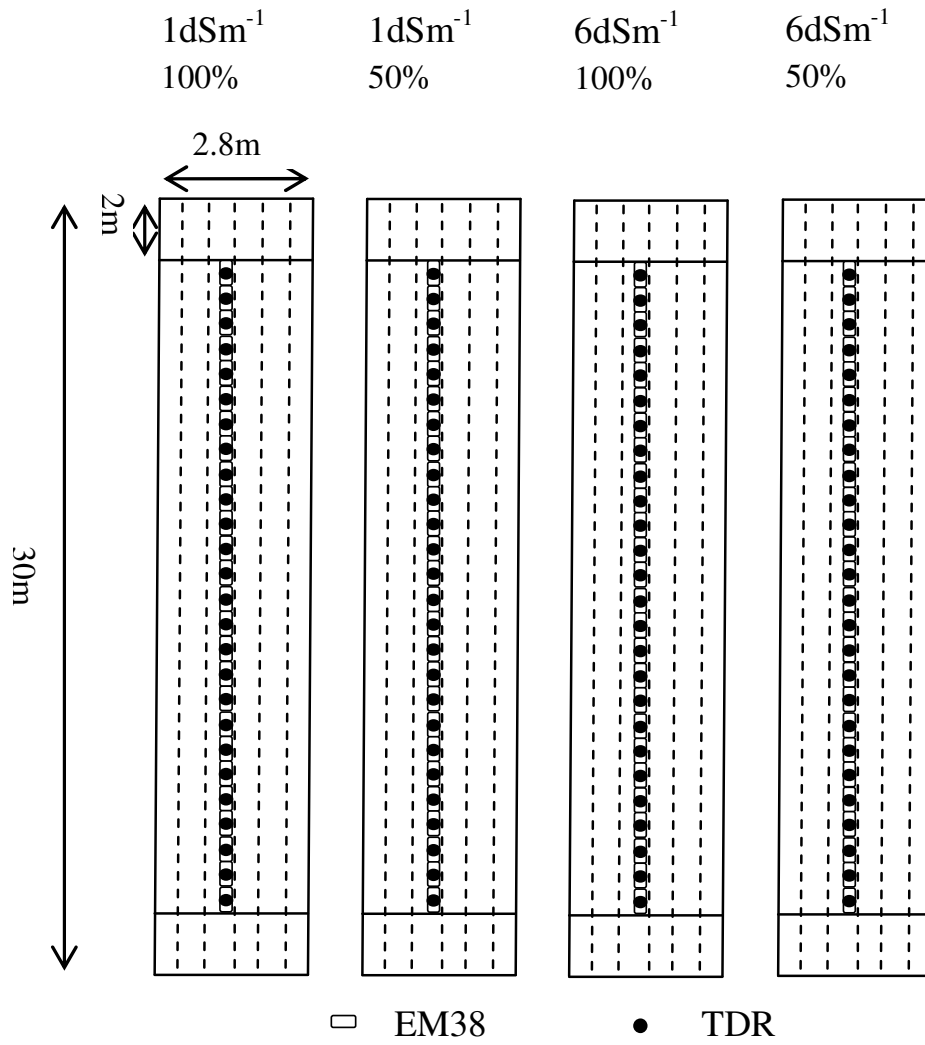
788 Von Hebel, C., S. Rudolph, A.Mester, J.A. Huisman, P. Kumbhar, H. Vereecken, and J. van der  
789 Kruk. 2014. Three-dimensional imaging of subsurface structural patterns using quantitative  
790 large-scale multiconfiguration electromagnetic induction data. *Water Resour. Res.* 50 (3):2732-  
791 2748.  
792

793 Wait, J.R. 1982. Geo-Electromagnetism. In *Geo-Electromagnetism*, 1-67. Academic Press.  
794

795 Ward, S.H., and G.W. Hohmann. 1988. Electromagnetic theory for geophysical applications.  
796 *Electromagnetic methods in applied geophysics*.  
797

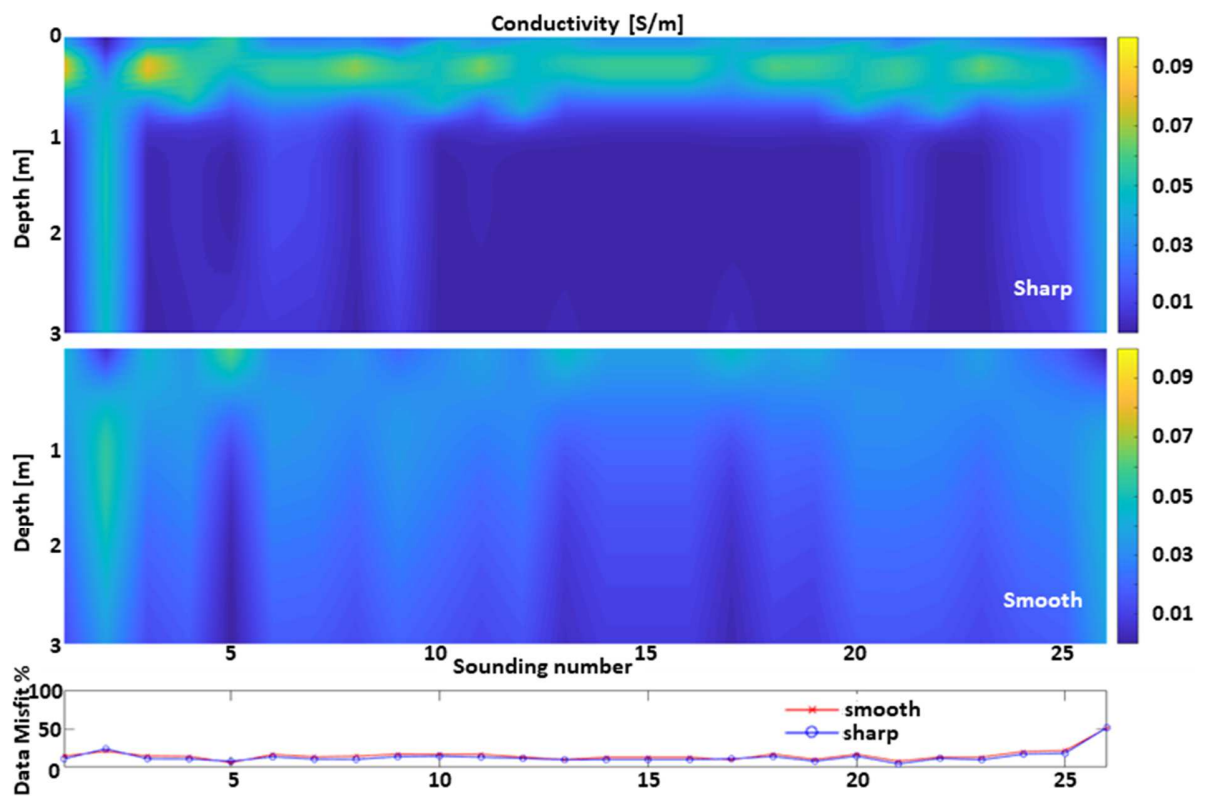
798 Weerts A. H., J. A. Huisman, and W. Bouten, .2001. Information content of time domain  
799 reflectometry waveforms. *Water Resources Research*. 37 (5), 1291–1299  
800

801 Wraith, J.M., B.L. Woodbury, W.P. Inskeep, and S.D. Comfort. 1993. A simplified waveform  
802 analysis approach for monitoring solute transport using time-domain reflectometry. *Soil Sci.*  
803 *Soc. Am. J.* 57 (3):637-642.  
804  
805 Yao, R., and Jingsong Y. 2010. Quantitative evaluation of soil salinity and its spatial distribution  
806 using electromagnetic induction method. *Agr. Water Manage.* 97 (12):1961-1970. doi:  
807 10.1016/j.agwat.2010.02.001.  
808  
809 Yu, M., and D.E. Dougherty. 2000. Modified total variation methods for three-dimensional  
810 electrical resistance tomography inverse problems. *Water Resour. Res.* 36 (7):1653-1664.  
811  
812 Zhdanov, M.S., G. Vignoli, and T. Ueda. 2006. Sharp boundary inversion in crosswell travel-time  
813 tomography. *J. Geophys. Eng.* 3 (2):122.  
814  
815 Zhdanov, M.S. 2002. *Geophysical Inverse Theory and Regularization Problems Methods.*  
816 Elsevier.  
817



818

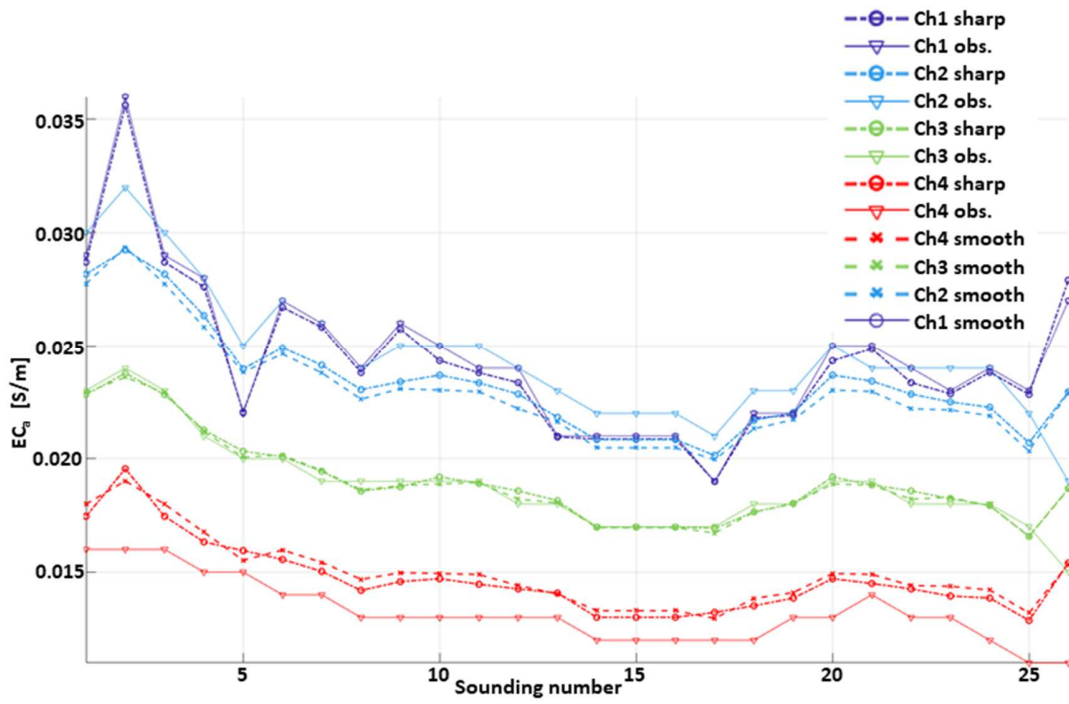
819 Figure 1. Schematic view of the experimental field



820

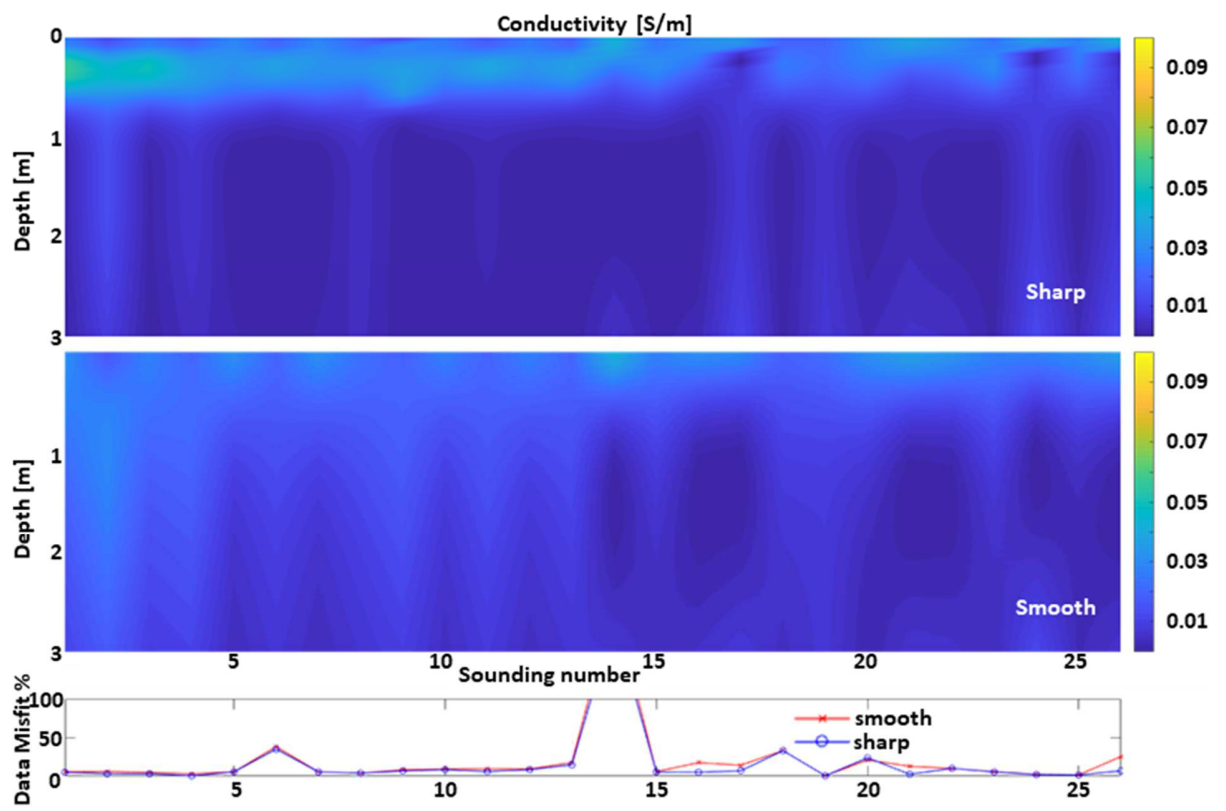
821 Figure 2. Examples of sharp and smooth inversions applied to the dataset 100-6dS. The results

822 are shown together with their corresponding data misfit.



823

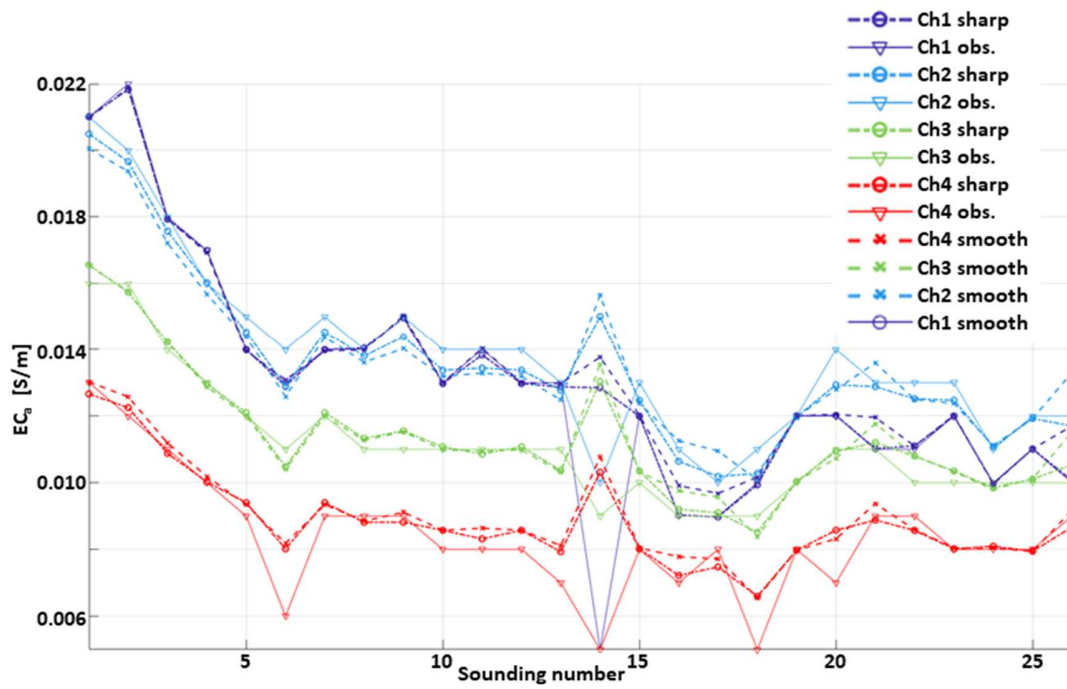
824 Figure 3. Comparison of the data fitting associated with the sharp and smooth inversions  
 825 applied to the dataset 100-6dS (Fig. 2). The calculated data corresponding to the sharp and  
 826 smooth results are shown together with the observations for each of the four measured  
 827 channels (heights).



828

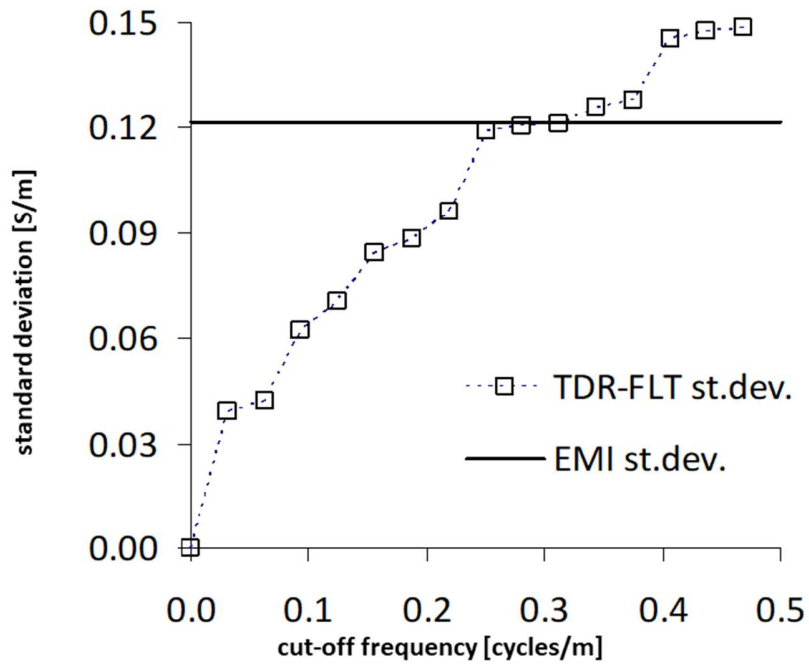
829 Figure 4. Examples of sharp and smooth inversions applied to the dataset 50-6dS. The results

830 are shown together with their corresponding data misfit.



831

832 Figure 5. Comparison of the data fitting associated with the sharp and smooth inversions  
 833 applied to the dataset 50-6dS (Fig. 4). The calculated data corresponding to the sharp and  
 834 smooth results are shown together with the observations for each of the four measured  
 835 channels (heights).



836

837 Figure 6. Standard deviation of the EMI series (horizontal black line) for the 50-6dS transect at  
 838 0.2-0.4 m depth. The squares show the corresponding standard deviations for the TDR series  
 839 for different level of filtering. The intersection of the EMI line with the TDR curve allows  
 840 identifying the optimal cut-off frequency range (~0.313 cycles/m) to make the two standard  
 841 deviations similar.

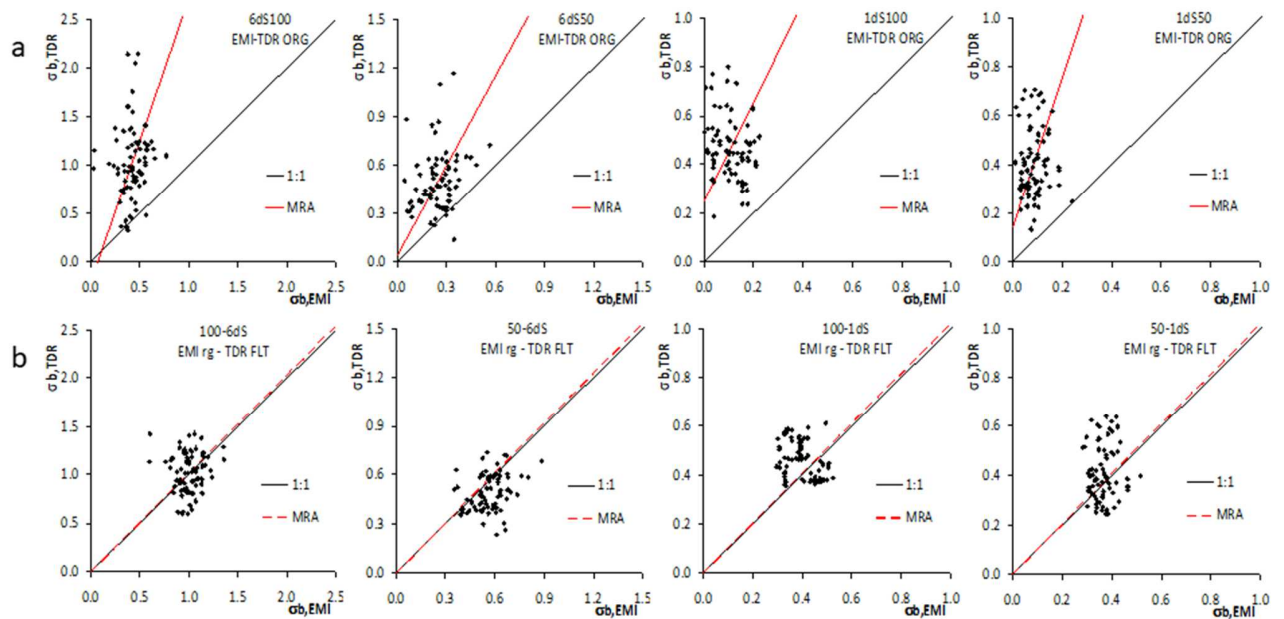


Figure 7. Comparison between  $\sigma_{b,TDR}$  and  $\sigma_{b,EMI}$  for all four transects for the depth range 0.0-0.6 m. The graphs in the top panels (a) show the original TDR and EMI data, while those in the bottom panels (b) the Filtered (FLT) TDR and EMI data after the regression based on MRA parameters (rg).

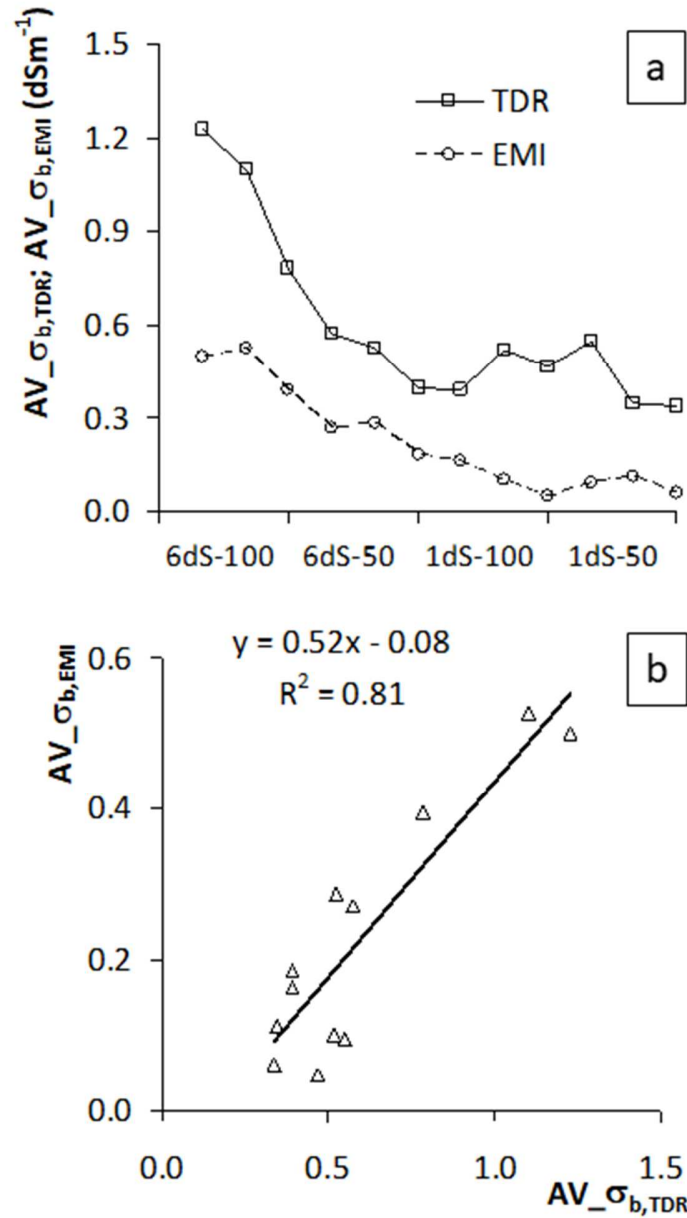


Figure 8. (a) Comparison of the means for the two original series (squares-solid line for TDR, dcircles-dashed line for EMI); (b) The same comparison on a 1:1 plot (triangles-solid regression line). In the panel (a), the four cases are shown in sequence. For each case, the three values are for the three depth intervals 0.0-0.2, 0.2-0.4, and 0.4-0.6 m.

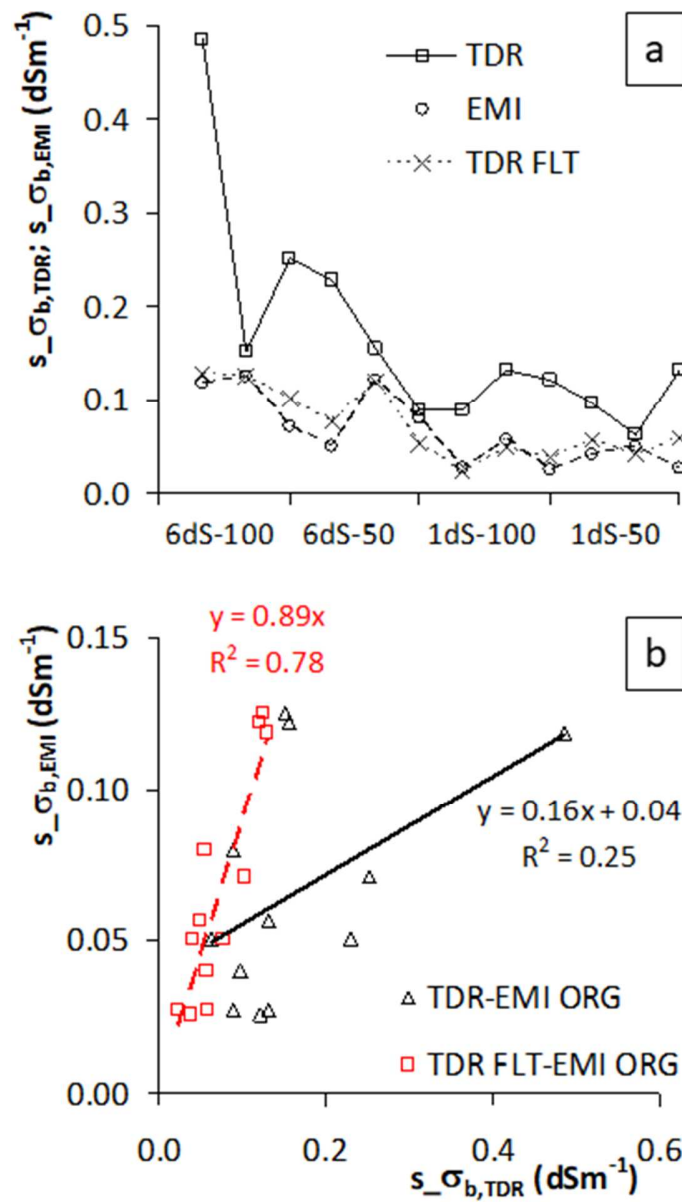


Figure 9. (a) Comparison of the standard deviations of the TDR original series (squares-solid line), of the EMI original series (circles-dashed line), and of the filtered (FLT) TDR series (crosses-dashed line); (b) The same comparison on a 1:1 plot: the original TDR and EMI data (triangles-solid regression line); filtered (FLT) TDR and original EMI data (squares-dashed regression line). In the panel (a), the four cases are shown in sequence. For each case, the three values are for the three depth intervals 0.0-0.2, 0.2-0.4, and 0.4-0.6 m.

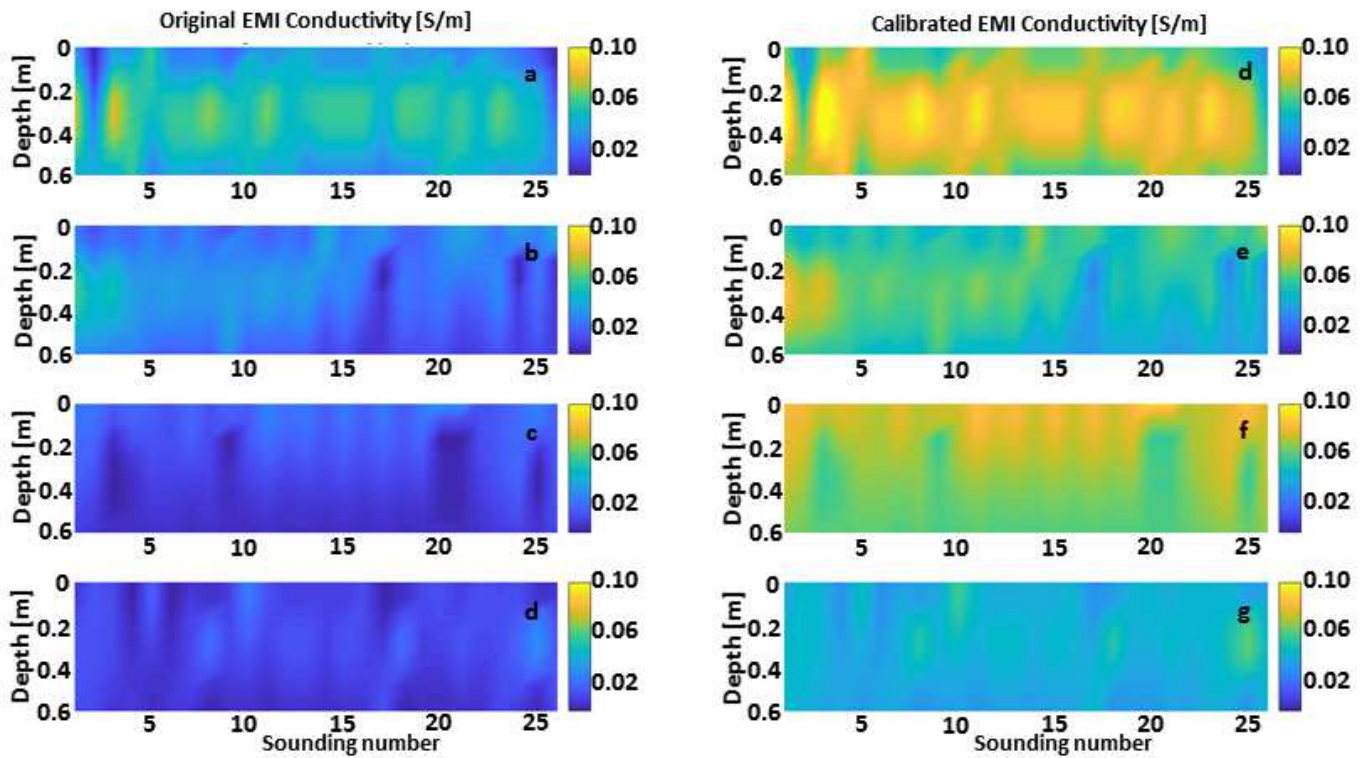


Figure 10. Maps of bulk electrical conductivity for the: (a) 100-6dS, (b) 50-6dS, (c) 100-1dS, (d) 50-1dS transects showing the original  $\sigma_{b,EMI}$  resulting from the inversion of the observed EMI data. Panels (d) to (g) show instead the corresponding results after the calibration via the TDR measurements (i.e., by applying Eq. 10).

<b>Transect</b>	<b>C<sub>b</sub></b>	<b>ρ<sub>L</sub></b>	<b>ρ<sub>P</sub></b>	<b>β</b>	<b>α</b>
<b>100-1dS</b>	0.10	0.02	0.33	2.04	0.25
<b>50-1dS</b>	0.10	0.00	0.08	3.06	0.14
<b>100-6dS</b>	0.18	0.02	0.07	2.92	-0.21
<b>50-6dS</b>	0.34	0.08	0.32	1.84	0.04

Table 1. Concordance parameters for the four transects for the TDR\_ORG and EMI\_ORG data. The table reports the Concordance,  $\rho_L$ , and the Pearson,  $\rho_P$ , correlation, as well as parameters  $\alpha$  and  $\beta$  of the MRA line. The bias factor,  $C_b$ , is also shown.

<b>Transect</b>	<b>C<sub>b</sub></b>	<b>ρ<sub>L</sub></b>	<b>ρ<sub>P</sub></b>	<b>β</b>	<b>α</b>
<b>100-1dS</b>	0.74	0.24	0.33	1.02	0.29
<b>50-1dS</b>	0.62	0.05	0.08	1.02	0.27
<b>100-6dS</b>	0.87	0.06	0.07	1.02	0.57
<b>50-6dS</b>	0.79	0.25	0.32	1.02	0.31

Table 2. Concordance parameters for the four transects for the TDR\_FLT and EMI\_ORG data. The table reports the Concordance,  $\rho_L$ , and the Pearson,  $\rho_P$ , correlation, as well as parameters  $\alpha$  and  $\beta$  of the MRA line. The bias factor,  $C_b$ , is also shown.